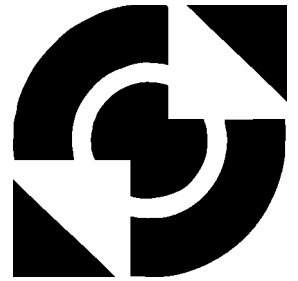


University of Twente

EEMCS / Electrical Engineering
Control Engineering



Modeling a Piezoelectric Inertial Stepping Turntable Using Bond Graphs

Martin Schepers

M.Sc. Thesis

Supervisors

Prof. dr. ir. J. van Amerongen

Dr. ir. S. Stramigioli

Ir. M. Patrascu

Ir. M. Bolks

September 2004

Report nr. 026CE2004

Control Engineering

EE-Math-CS

University of Twente

P.O. Box 217

7500 AE Enschede

The Netherlands

Abstract

The limits of the current hard disk technology are coming in sight. One of the projects which aims at overcoming these limits is the micro Scanning Probe Array Memory ($\mu SPAM$) project at the University of Twente.

A main component in the $\mu SPAM$ project is a stick-slip driven turntable, which is able to align an object (the read/write medium) with respect to another object (the read/write probes). In order to investigate the influence of different factors (e.g. size, materials) and to facilitate the future design of a controller, a model of the turntable has been developed.

This report presents a bond graph model of the turntable which consists of submodels representing the main components of the turntable. The piezoelectric tubes have been modeled by variable spatial springs in combination with 2-port C-elements. The stick-slip motion has been modeled with the Generalized Maxwell Slip (GMS) friction model, implemented at the contact surfaces between the tubes and the table.

In order to validate the developed bond graph model, measurements have been done on the real turntable which have been compared to simulations. The comparison shows that the general behaviour of the turntable is approximated by the developed model.

Preface

This report represents the final thesis for completing my Master of Science study in the field of Electrical Engineering at the University of Twente.

I would like to thank some people for their support during this assignment. First I would like to thank Mihai Patrascu for all the effort he has put in helping me to complete this assignment. Stefano Stramigioli deserves a lot of appreciation for all the advice he gave during the modeling process. Furthermore I would like to thank Mathieu Bolks for giving the opportunity to do measurements on his turntable setup and assisting me during the measurements.

Enschede, September 24, 2004

Martin Schepers

Contents

1	Introduction	1
2	Setup	3
2.1	Piezoelectric Tubes	4
2.2	Friction	9
3	20-sim Model	17
3.1	Geometry	17
3.2	Piezoelectric Tube Model	19
3.3	Contact Model with Friction	25
3.4	Complete Model of the Turntable	29
4	Measurements and Simulations	31
4.1	Measurements	31
4.2	Simulations	36
4.3	Discussion	38
5	Conclusions and Recommendations	39
5.1	Conclusions	39
5.2	Recommendations	39
A	Energy Function of the Piezoelectric Element	41
B	Spring Constants of the Tube	42
B.1	Bending Stiffness	43
B.2	Elongation Stiffness	43
B.3	Torsional Stiffness	43
C	Mass Properties	44
C.1	Mass	44
C.2	Mass Moment of Inertia	44
C.3	Center of Mass of the Table	46
D	Parameters	48

Chapter 1

Introduction

With the growing demand to increase the speed and capacity of hard disks, the limits of the current technology come in sight. Slowly but surely, data density and especially read/write access times are saturating. In order to overcome this, a lot of effort is put in developing new methods and media for mass storage systems. One of these is the $\mu SPAM$ ¹ project at the University of Twente. The development efforts will lead to a product of which the specifications are expected to lie in between those of flash memory and actual hard disk technology. This means more capacity than flash memory and much smaller access times compared to hard disks.

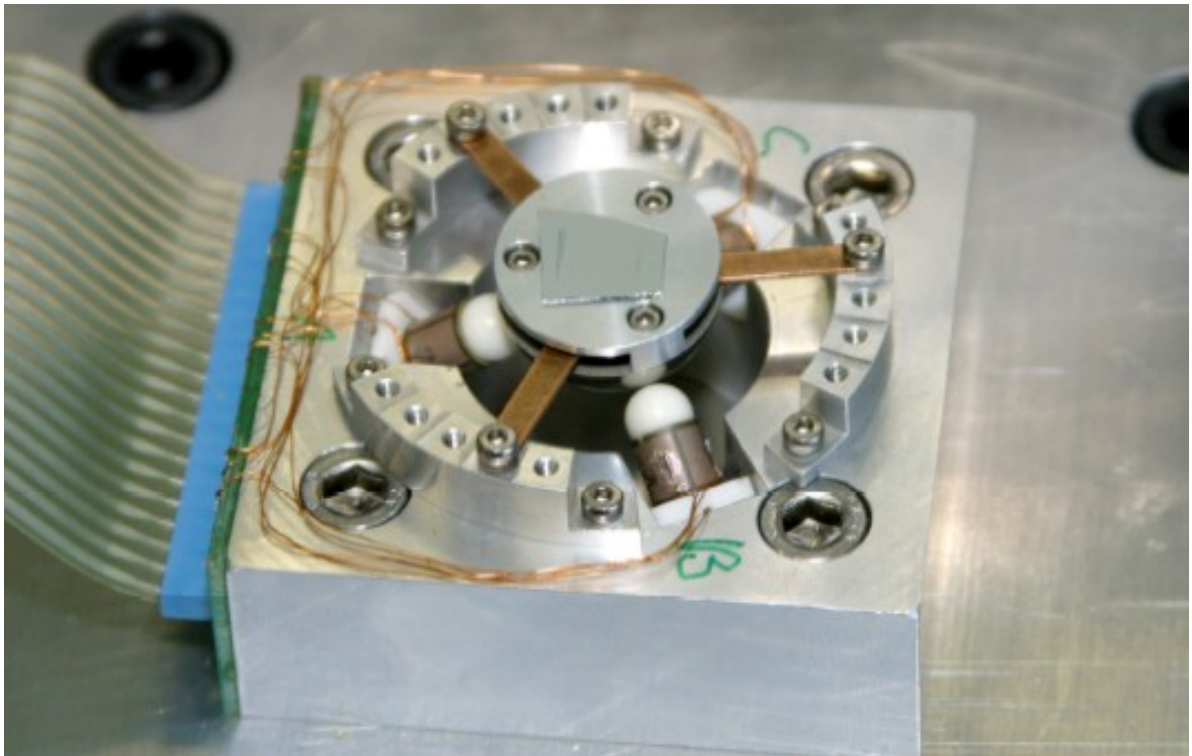


Figure 1.1: Picture of the turntable.

¹ $\mu SPAM$ stands for micro Scanning Probe Array Memory, more information about the project can be found at: <http://www.uspam.nl>

This assignment is part of the μ SPAM project and is about a turntable which is able to align an object with respect to another object. By rotating the turntable around three rotational axes, the read/write medium can be aligned with respect to the read/write probes.

A picture of the turntable is shown in Figure 1.1. The main components are the table itself (the half sphere) and the three piezoelectric tubes. The rotations are achieved by using Inertial Sliding Motion (ISM) [19] [10] in which the stick-slip effect plays a central role. An example of the stick-slip effect is the way a pizza is put into the oven at a pizzeria. With a slow movement the pizza is lead into the oven and the pizza ‘sticks’ to its support. With a fast movement the support is pulled out of the oven and the pizza ‘slips’ over its support and stays in the oven. The actuation of the turntable is based on the same principle. By bending the tubes at slow speed, the table sticks to the tubes and follows the movement of the tubes due to the friction. By pulling the tubes back to their starting position at high speed, the table ‘slips’ over the tubes due to the inertia. The net result is a rotational movement of the table.

The main objective of this assignment is to develop a model of the turntable and simulate the rotations around the three axes. The model has been implemented in 20-sim² with screw bond graphs. Screw bond graphs represent an energy based approach and provide a means for modeling, independent of the physical domain of the model. This means the electrical and mechanical domain can be combined into one and the same model in an energy consistent way.

This report is organized as follows. A description of the turntable setup is given in Chapter 2 and the most important parts are discussed in detail. Chapter 3 describes the 20-sim simulation model developed, which is built from several submodels of the different parts of the turntable. Chapter 4 is about the performed measurements and simulations, and discusses the results. The report is finalized with conclusions and some recommendations.

²20-sim is a powerful modeling and simulation package developed by Controllab Products B.V.: <http://www.20sim.com>

Chapter 2

Setup

The turntable setup, which is shown in Figure 2.1, will be described in this chapter. The turntable is in fact a half sphere, which rests on three smaller balls. The balls are connected to piezoelectric tubes, which are able to bend. The tubes are positioned perpendicular to each other and their central axes intersect at the top of the half sphere. Furthermore there is a preloading spring on top of the half sphere, which assures good contact between the balls and the half sphere (not visible in Figure 2.1). The turntable is able to rotate around each of the three tube axes as well as around the z -axis (the z -axis is perpendicular with respect to the ground). The rotations of the turntable are achieved using the stick-slip effect. A slow motion of the piezoelectric tubes in one direction is followed by an abrupt jump in the opposite direction. During the slow period, the table follows the tubes because of friction, whereas it cannot follow the sudden jump back because of the inertia.

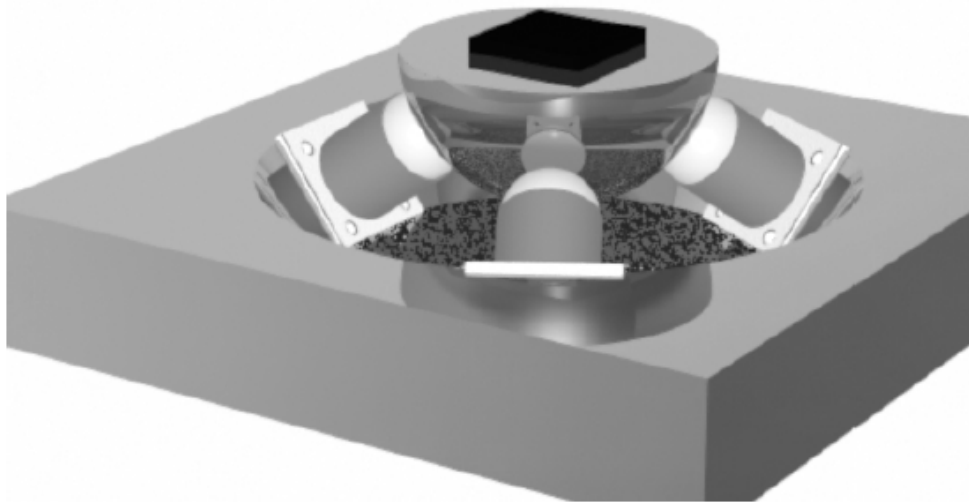


Figure 2.1: Schematic view of the turntable.

This chapter describes some of the elements of the turntable and the theory behind it. Section 2.1 describes the piezoelectric tubes. It first gives some general information about the tubes, followed by some background theory on piezoelectricity and the section ends with the bending equations of the tube. Section 2.2 is about friction. The section starts with some general information about friction, after which the results of a short literature survey on existing friction models are shown. The section concludes with a motivation for the chosen friction model to be used in the bondgraph model of the turntable.

2.1 Piezoelectric Tubes

The turntable is being rotated using piezoelectric tubes. The turntable uses piezoelectric tubes manufactured by PI Ceramic and are made of PIC 151 material, which is a material characterized by a high piezoelectric coupling factor, a very high dielectric constant and consequently a high piezoelectric constant [6].

The piezoelectric tubes used for the turntable are hollow cylinders made of PZT, metallized on the outer and inner surfaces and poled in radial direction (Fig. 2.2). The outside metal coating is sectioned into four quadrants. By applying a voltage on one (asymmetric mode) or two (symmetric mode) quadrants, the PZT material between the actuated electrodes will elongate resulting in tube bending.

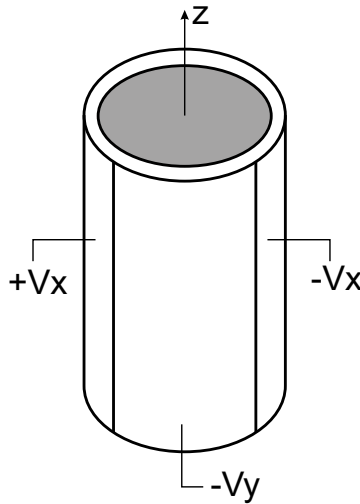


Figure 2.2: Piezoelectric Tube.

The next paragraph is about piezoelectricity. The theory behind piezoelectricity will be described and the constitutive relations will be derived. These relations are then written in terms of the power-conjugated variables used in the bondgraph model. The paragraph ends with the co-energy function of the piezoelectric element. Paragraph 2.1.2 describes the bending of the tubes in detail. Due to an elongation of the piezoelectric elements, the tubes bend along a circular path. This circular path can be described with a radius of curvature. The paragraph concludes with an expression for this radius in terms of the piezoelectric element parameters.

2.1.1 Piezoelectricity

Piezoelectricity is the ability of certain crystalline materials to convert mechanical energy into electric energy and vice versa. The *direct* piezoelectric effect is that, when subjected to mechanical stress (force per unit area), these materials generate an electric charge proportional to the stress applied. The *inverse* piezoelectric effect is that the same materials become strained (elongation per unit length) when an electric field is applied, the strain again being proportional to the applied field. Piezoelectric sensors exploit the direct effect, whereas piezoelectric actuators rely on the inverse effect.

The piezoelectric tubes used in the turntable are made of Lead (Plumbum) Zirconate Titanate (PZT), which is a piezoceramic material. Above a temperature known as the Curie temperature, the elementary cells of this material have a cubic lattice and no dipole moment. An elementary cell with the cubic structure is shown at the left of Figure 2.3. Below the Curie

temperature the elementary cells take on a tetragonal lattice in which a dipole is present (at the right in Figure 2.3). Neighbouring dipoles align with each other to form regions of local alignment and therefore resulting in a dipole moment. A stress (tensile or compressive) applied to such a crystal will alter the separation between the positive and negative charge sites in each elementary cell leading to a net polarization at the crystal surface [20].

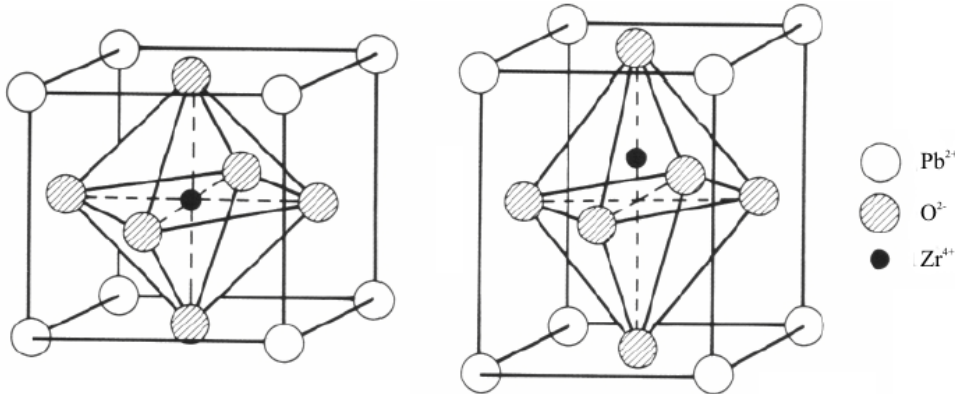


Figure 2.3: PZT elementary cell with cubic (left) and tetragonal (right) lattice.

For piezoelectric materials, the electrical and mechanical constitutive equations are coupled. It is convenient to assign numbers to the different directions of deformations as shown in Figure 2.4. Immediately after applying a voltage to the piezoelectric element in the 1-direction, a strain $S_3 = d_{31}E_1 = d_{31}V/h$ in the 3-direction is generated. It in turn creates a stress $T_3 = S_3/s_{33}$ in the 3 direction, where s_{33} is the compliance. The same holds for the electric displacement D_1 . After applying a force to the piezoelectric element, an electric displacement, $D_1 = d_{31}T_3 = d_{31}F/A_m$ is generated. It in turn creates an electric field $E_1 = D_1/\epsilon_{11}$ in the 1 direction, where ϵ_{11} is the permittivity. The resulting constitutive equations are shown in Equation 2.1.

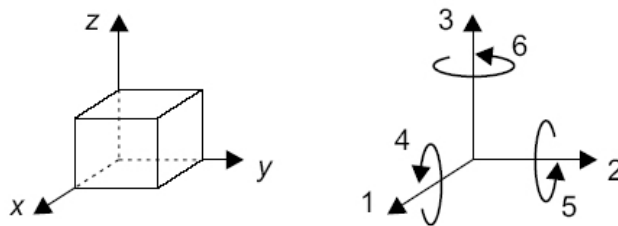


Figure 2.4: Designation of the axes and directions of deformation.

$$\begin{pmatrix} S_3 \\ D_1 \end{pmatrix} = \begin{pmatrix} s_{33}^E & d_{31} \\ d_{31} & \epsilon_{11}^T \end{pmatrix} \begin{pmatrix} T_3 \\ E_1 \end{pmatrix}, \quad (2.1)$$

with:

- d_{31} [C/N] or [m/V] piezoelectric charge constant, which relates either the strain S in direction 3 to the electric field E in direction 1 in the absence of mechanical stress, or the electric displacement D in direction 1 to the stress T in direction 3, in a zero electric field;

- s_{33}^E [m^2/N] the compliance for constant electric field E ;
- ϵ_{11}^T [F/m] the permittivity under constant stress T .

Equation 2.1 shows the general form of the piezoelectric material, whereas Equation 2.2 shows the equations for the power-conjugated variables used in the simulation model:

- The tensional force applied to the element, along the z -axis: $F = A_m T_3$, where A_m is the elongated surface;
- The expansion of the element, along the z -axis: $z = L S_3$, where L is the length of the tube;
- The voltage applied to the electrodes: $V = h E_1$, where h is the wall thickness of the tube;
- The charge at the electrodes: $q = A_e D_1$, where A_e is the actuated surface.

$$\begin{pmatrix} z \\ q \end{pmatrix} = \begin{pmatrix} \frac{s_{33}^E L}{A_m} & \frac{d_{31} L}{h} \\ \frac{d_{31} L}{h} & \frac{\epsilon_{11}^T A_e}{h} \end{pmatrix} \begin{pmatrix} F \\ V \end{pmatrix}, \quad (2.2)$$

with $A_e = \frac{\pi D L}{4}$ and $A_m = \frac{\pi D h}{4}$ and therefore $\frac{A_e}{A_m} = \frac{L}{h}$.

The co-energy function of the piezoelectric element can be derived from the above relations. The derivation is shown in Appendix A and the resulting equation is:

$$E^*(F, V) = \frac{s_{33}^E L}{2 A_m} F^2 + \frac{\epsilon_{11}^T A_e}{2 h} V^2 + \frac{d_{31} L}{h} F V. \quad (2.3)$$

2.1.2 Tube Bending Equations

This paragraph describes the derivation of the bending equations of the tubes. This is accomplished by looking at the stress and strain distribution in the wall of the tube. From this distribution, the location of the neutral plane (zero stress) is derived. By using some geometry relations, the radius of curvature describing the bending is derived. The radius of curvature is used to derive the expression for the deflection of the tube.

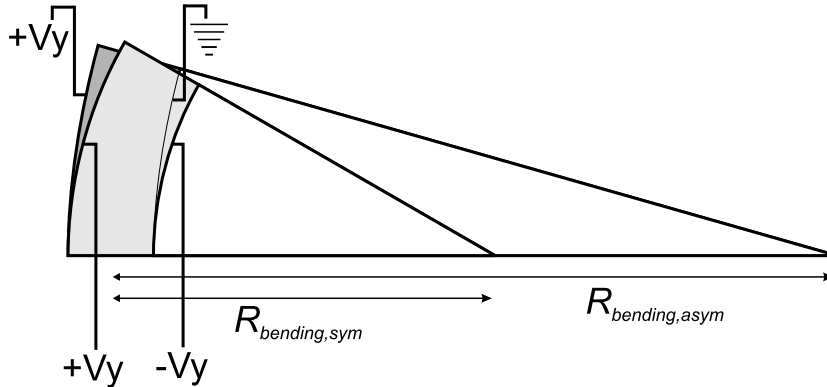


Figure 2.5: Tube bending in asymmetric and symmetric mode.

To obtain the relations describing the bending of the tube, Figure 2.5 and 2.6 are used. Figure 2.5 shows the bending of the tube in the symmetric as well as the asymmetric voltage mode. In the symmetric voltage mode two voltages equal in magnitude and opposite in sign ($+Vy$ and $-Vy$) are applied to two opposite quadrants, while the other two quadrants are

grounded (not shown in the figure). Conversely, in the asymmetric voltage mode only one quadrant is actuated. From the figure it becomes clear that the radius of curvature $R_{bending}$ in the asymmetric mode is twice the radius in the symmetric mode. Although the turntable is used in the asymmetric voltage mode, the relations are derived for the symmetric mode. This is because it is much easier to derive the stress and strain relations in the symmetric mode. As a consequence of symmetry, the resulting deflection for the asymmetric mode is one-half of the deflection in the symmetric mode [7].

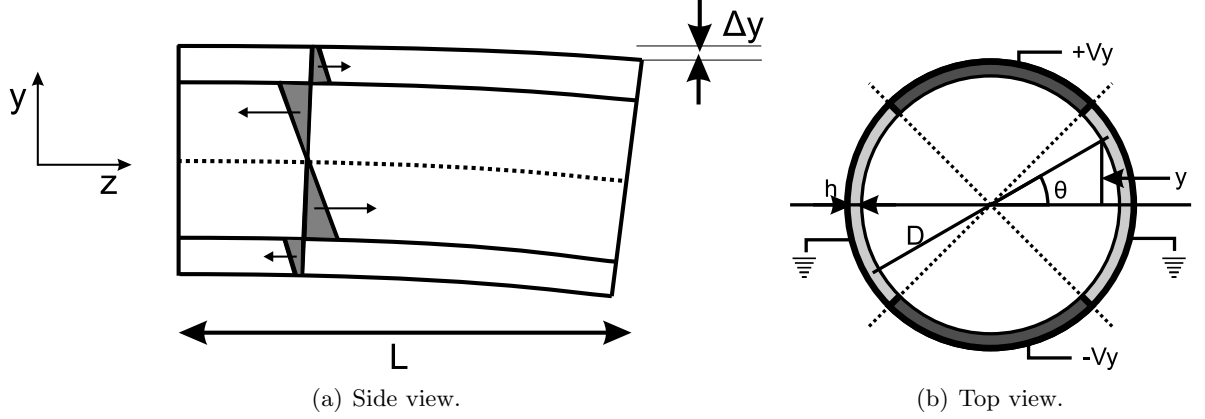


Figure 2.6: Bending of the piezoelectric tube in symmetric mode.

The wall thickness h of the piezoelectrics is usually much smaller than the diameter D of the tube. Therefore, the variation of stress and strain over the wall thickness can be neglected. As shown in Figure 2.6, two voltages equal in magnitude and opposite in sign are applied to the two y quadrants and the two x quadrants are grounded. The onset of the y voltages results in stress and strain in the z direction, which causes the tube to bend. The bending of the tube generates a torque in the opposite direction. At equilibrium, the total torque in any cross section is zero. For reasons of symmetry, it is sufficient to consider one quarter of the tube ($0 < \theta < \frac{\pi}{2}$) and it is assumed that the stress generated by the bending is linear with respect to y [7]. The total stress $T(\theta)$ as a function of angle θ is therefore:

$$\begin{aligned} 0 < \theta < \frac{\pi}{4}, \quad T(\theta) &= -\alpha \sin \theta \\ \frac{\pi}{4} < \theta < \frac{\pi}{2}, \quad T(\theta) &= T_3 - \alpha \sin \theta. \end{aligned} \quad (2.4)$$

The constant α is to be determined from the condition of zero torque. The total torque can be found by integrating over the whole area and recalling that the variation of strain and stress over the wall thickness has been neglected. This results in:

$$\begin{aligned} \tau_{tot} &= \int_A T y dA = \int_{\theta} T \sin \theta d\theta = 0 \\ \int_0^{\frac{\pi}{4}} (-\alpha \sin \theta) \sin \theta d\theta + \int_{\frac{\pi}{4}}^{\frac{\pi}{2}} (T_3 - \alpha \sin \theta) \sin \theta d\theta &= 0, \end{aligned} \quad (2.5)$$

which gives:

$$\alpha = \frac{2\sqrt{2}T_3}{\pi}. \quad (2.6)$$

By assuming again that the stress generated by bending is linear with respect to y , the neutral plane ($T = 0$) can be found by extrapolating the stress distribution:

$$\begin{aligned} T\left(\frac{\pi}{4}^+\right) &= T_3 - \alpha \sin\left(\frac{\pi}{4}\right) = T_3\left(1 - \frac{2}{\pi}\right) & @ & \quad y = \frac{D\sqrt{2}}{4} \\ T\left(\frac{\pi}{2}\right) &= T_3 - \alpha \sin\left(\frac{\pi}{2}\right) = T_3\left(1 - \frac{2\sqrt{2}}{\pi}\right) & @ & \quad y = \frac{D}{2}, \end{aligned} \quad (2.7)$$

which gives for the neutral plane at zero stress:

$$y_0 = \frac{\pi D}{4\sqrt{2}} \approx 0.555D. \quad (2.8)$$

From Figure 2.7 and the definition of strain S_3 , the curvature of bending $R_{bending}$ can be found:

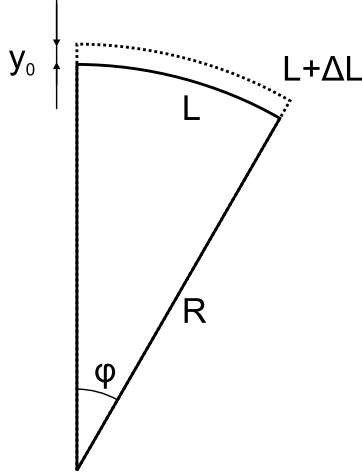


Figure 2.7: Curvature of bending.

$$S_3 = \frac{\Delta L}{L} = \frac{(L + \Delta L) - L}{L} = \frac{(R + y_0)d\varphi - Rd\varphi}{Rd\varphi} = \frac{y_0}{R}, \quad (2.9)$$

and therefore:

$$R_{bending} = \frac{y_0}{S_3} = \frac{\pi Dh}{4\sqrt{2}d_{31}V}. \quad (2.10)$$

Now the deflection Δy (shown in Fig. 2.6), assuming $\Delta y \ll L$, is found to be:

$$\Delta y = \frac{L^2}{2R_{bending}} = \frac{2\sqrt{2}d_{31}VL^2}{\pi Dh}. \quad (2.11)$$

For reasons of symmetry, the formula for the x deflection has the same form.

As mentioned in the introduction of this paragraph (Figure 2.5), the deflection of the tube when applying a voltage to only one of the four quadrants, equals exactly one-half of the deflection when applying two equal and opposite voltages to two quadrants. This means the radius $R_{bending}$ in the asymmetrical mode will be twice the radius in the symmetrical mode and is therefore given by:

$$R_{bending} = \frac{\pi Dh}{2\sqrt{2}d_{31}V}. \quad (2.12)$$

$R_{bending}$ is the radius of curvature describing the bending in the asymmetric voltage mode. This radius is used in Paragraph 3.2.2 to modulate the length of the 3D spring in 20-sim.

2.2 Friction

Several models have been developed to describe frictional behaviour [1], [2] and [13]. This section shows the result of a short literature survey and gives an overview of different friction models with their advantages and disadvantages. The section ends with a paragraph about the friction model chosen to be used in the bond graph model and a motivation why it has been chosen.

2.2.1 General Terms

Friction is a well known problem and has a highly nonlinear character. Friction is the result of interactions between the surfaces of materials in contact. In the classical models of friction, the friction force is a function of the relative velocity between the objects. However, this is not always the case, because the friction force can also be a function of the displacement. In this way, one could define two friction regimes: the presliding regime (friction force as function of the displacement) and the sliding regime (friction force as function of the velocity). This paragraph describes the main properties of friction, starting with friction at asperity contacts and the two friction regimes. After that the Stribeck curve is introduced, which assures a smooth transition between the two regimes. The end of this paragraph describes some important friction phenomena like hysteresis, nonlocal memory and drift.

In the presliding regime, the adhesive forces at asperity contacts are dominant such that the friction force appears to be a function of displacement rather than velocity. The asperities, which can be seen as little bristles, behave like springs which will break when a certain threshold force is exceeded. As the displacement increases, more and more asperities will break resulting eventually in gross sliding. In the sliding regime all the asperities are broken such that the friction force is a function of the velocity. Accurate modeling and control of mechanical systems with friction requires a model which includes both regimes.

The presliding regime is known as the ‘stick’ phase and the sliding regime is known as the ‘slip’ phase. The maximum friction force at the beginning of sliding is called the break-away force or the static friction force. The friction in the sliding regime is generally called kinetic friction.

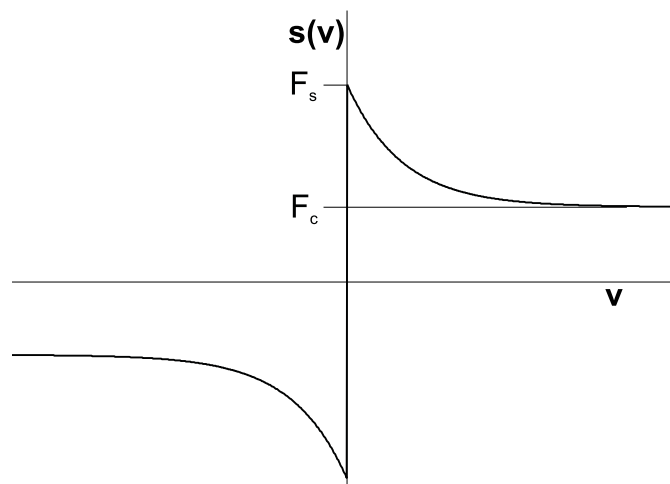


Figure 2.8: Stribeck Curve.

Stribeck [17] derived a relation which describes the velocity dependent friction force continuously and is known as the Stribeck curve. The curve is shown in Figure 2.8 and the relation is given by:

$$s(v) = \text{sgn}(v) \left(F_c + (F_s - F_c) e^{-|v/v_S|^{\delta_{v_S}}} \right), \quad (2.13)$$

with F_s the static friction force, F_c the Coulomb force, v_S the Stribeck velocity and δ_{v_S} the Stribeck shape factor. The friction force increases for decreasing velocities to the static friction force.

Both F_s and F_c depend on the normal force at the contact surface:

$$\begin{aligned} F_s &= \mu_s F_N \\ F_c &= \mu_c F_N, \end{aligned} \quad (2.14)$$

with μ_s the static friction coefficient and μ_c the dynamic friction coefficient.

As mentioned before, the friction force is a function of the displacement in the presliding regime and the displacement is characterized by elastic behaviour. However, when the applied tangential force becomes larger, some asperities will go into the slip phase, while others stay in the stick phase. This means, the friction force is not proportional to the displacement and the presliding regime will show hysteresis behaviour. Furthermore, this hysteresis behaviour has nonlocal memory, which means the force at any instant in time not only depends on the values at some time instant in the past, but also on the past extremum values of the force and the displacement. In other words: by closing an inner loop of the hysteresis curve, the curve returns to the outer loop. This nonlocal memory property is shown in the hysteresis curve of Figure 2.9.

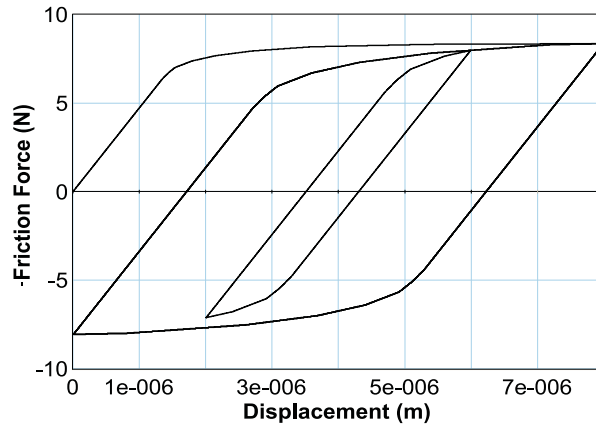


Figure 2.9: Hysteresis Curve with nonlocal memory.

Many friction models suffer from drift [9], which means there is some irreversible displacement in the stick-phase. A model can be tested on the drifting property by looking at the friction when an object moves over a surface. By first applying a friction force large enough to bring the object in the slip phase and then back into the stick phase with an extra oscillation on the force signal in the stick phase. A model incorporating the drifting property will first show a displacement of the object due to slipping over the surface and no displacement when the object is in the stick-phase with the oscillatory force applied. Paragraph 2.2.3 describes the testing on the drifting property for two different friction models.

2.2.2 Existing Friction Models

This section shows some existing friction models with their advantages and disadvantages. The models have been divided in static and dynamic models, based on dual variables. This means the dynamic models contain a state, whereas the static models do not. First some static models will be described, followed by some dynamic friction models.

Static Friction Models

As mentioned, a short summary of some static friction models is given first.

- **Classical models of friction** describe a static relationship between the friction force and the velocity for non-zero velocities. A general description of static friction models is:

$$F_f = \begin{cases} s(v) + \sigma_2 v & \text{if } v \neq 0 \\ F_a & \text{if } v = 0 \text{ and } |F_a| < F_s, \\ F_s \text{sgn}(F_a) & \text{otherwise,} \end{cases} \quad (2.15)$$

with F_a the external force applied to the system, F_s the static force, σ_2 the viscous friction coefficient and $s(v)$ the Stribeck curve, which has been mentioned in the previous paragraph (Figure 2.8).

- **Karnopp** [11] defined a small interval of zero velocity to overcome the problems with zero velocity detection and to avoid switching between different state equations for sticking and sliding. For velocities within this interval the internal state of the system (the velocity) may change and be non-zero but the output of the block is maintained at zero by a dead-zone. The friction force is either a static friction force (inside the interval) or an arbitrary static function of velocity (outside the interval). The main drawback of the model is that it is strongly coupled with the rest of the system. The external force is an input to the model and this force is not always explicitly given.
- **Breedveld** [4] describes a port-based friction model, which is an extension of the Karnopp model. The friction force consists of a static as well as a dynamic component. The static component is characterized by the break-away force, the dynamic component is characterized by the Coulomb force. An advantage compared to other models, e.g. Karnopp model, is that the momentum of the two objects in the stick phase can still change. The transition from stick to slip is based on a force criterion, whereas the transition from slip to stick is based on a velocity criterion. Breedveld describes two versions: A model with a preslip velocity and a model without a preslip velocity. The main drawback of the model without a preslip velocity is that the model is dependent on other objects in the model and will therefore not be described. The model with a preslip velocity is shown in Equation 2.16 and 2.17.

$$F_f = \begin{cases} F_{st} \frac{v(t_k)}{v_{preslip}} & \text{if } [|v(t_k)| < v_{preslip}] \wedge \text{not } slip(t_{k-1}) \\ F_c \text{sgn}(v(t_k)) & \text{otherwise;} \end{cases} \quad (2.16)$$

$$slip(t_k) = \begin{cases} \text{true} & \text{if } |v(t_k)| > v_{preslip}, \\ \text{false} & \text{if } |v(t_k)| < 0.1 * v_{preslip}, \\ slip(t_{k-1}) & \text{otherwise,} \end{cases} \quad (2.17)$$

where $v_{preslip}$ is the velocity margin near the origin before the slip phase starts. The model always has a static causality and a linear relation between the friction force and

velocity. Another advantage is that the model is easy to implement. A drawback is that a simulation with a fixed step simulation algorithm together with a relatively small preslip velocity may become inefficient. Furthermore the model is not able to minimize drift and does not cover the presliding behaviour (hysteresis).

Dynamic Friction Models

Subsequently, several dynamic friction models are presented.

- **Dahl** proposed a friction model, which models the stress-strain curve by a differential equation. The model is described in [3]. This friction model describes a constant friction (equal to the static friction) in the sliding regime and it produces a smooth transition around zero velocity. The friction hysteresis at pre-sliding is approximated by a first order equation of the position depending only on the sign of the velocity. Dahl proposed the following equation:

$$\frac{dF_f}{dx} = \sigma_0 \left| 1 - \frac{F_f}{F_s} \operatorname{sgn}(v) \right|^{\delta_d} \operatorname{sgn} \left(1 - \frac{F_f}{F_s} \operatorname{sgn}(v) \right), \quad (2.18)$$

with σ_0 the initial stiffness of the contact at velocity reversal and F_s equal to the static friction force (for this model F_s equals F_c , the Coulomb friction force). The exponent δ_d is a model parameter determining the shape of the hysteresis. The Dahl model predicts position dependent hysteresis loops, but the model neither predicts a break-away force, nor includes the Stribeck effect and frictional lag. Furthermore the model is not able to minimize drift.

- **The LuGre model** [5] combines the Dahl model with characteristics like the Stribeck curve. The friction force is modeled by bending asperities behaving like springs. However, the deflection of the asperities is based on the average behaviour instead of modeling the random behaviour. The average deflection of the asperities is denoted as z and is modeled as:

$$\frac{dz}{dt} = v - \sigma_0 \frac{v}{s(v)} z. \quad (2.19)$$

The friction force is given as a function of the state variable z and velocity v by:

$$F_f = \sigma_0 z + \sigma_1 \frac{dz}{dt} + \sigma_2 v. \quad (2.20)$$

The first term in Equation 2.19 gives a deflection that is proportional to the integral of the velocity. For the second term, for constant velocities, $s(v)$ is given by $s(v) = \sigma_0 v$ and therefore the friction force in Equation 2.20 is given as the Stribeck curve plus the viscous term. In the general case, the friction force is a superposition of terms proportional to the deflection, the rate of deflection and a viscous term. The LuGre model captures the Stribeck curve and frictional lag in the sliding regime, it approximates the hysteresis curve in the pre-sliding regime and it is able to simulate the break-away force at transition from pre-sliding to sliding. However the model is not able to minimize drift and there is a damping term present in Equation 2.20, $(\sigma_1 \frac{dz}{dt})$, which is physically not obvious.

- **The elasto-plastic friction model** introduced by Dupont [9], is a general one-state friction model that is stable, dissipative and incorporates pre-sliding displacement and

the drifting property. It is an extension of the LuGre friction model where the friction force equation remains the same, but the state equation becomes:

$$\frac{dz}{dt} = v - t(z, v)\sigma_0 \frac{v}{s(v)}z, \quad (2.21)$$

and

$$t(z, v) = \begin{cases} 0 & \text{if } |z| \leq z_{ba} \text{ or } \text{sgn}(v) \neq \text{sgn}(z) \\ \frac{1}{2} \sin\left(\pi \frac{z - (\frac{z_{ss}(v) + z_{ba}}{2})}{z_{ss}(v) - z_{ba}}\right) + \frac{1}{2} & \text{if } z_{ba} \leq |z| \leq z_{ss}(v) \\ 1 & \text{if } |z| \geq z_{ss}(v), \end{cases} \quad (2.22)$$

with $0 < z_{ab} < z_{ss}(v) = |s(v)/\sigma_0|$.

The advantage of the elasto-plastic model is its ability to minimize (unrealistic) drift. No drift occurs if $|z| < z_{ba}$ and under this condition the pre-sliding behaviour corresponds to a linear spring-damper system.

- **The Leuven model** [12] is an extension of the LuGre model, incorporating a hysteresis function with nonlocal memory in the pre-sliding regime. As in the LuGre model, the model uses a state variable z which can be seen as the average deflection of the asperity junctions:

$$\begin{aligned} F_f &= F_h(z) + \sigma_1 \frac{dz}{dt} + \sigma_2 v, \\ \frac{dz}{dt} &= v \left(1 - \text{sgn}\left(\frac{F_d(z)}{s(v) - F_b}\right) \left| \frac{F_d(z)}{s(v) - F_b} \right|^{\delta_l} \right). \end{aligned} \quad (2.23)$$

The Leuven shape factor δ_l determines the friction force during transition from pre-sliding to sliding and $F_h(z)$ is the hysteresis force.

- **The Generalized Maxwell-slip friction model** [12] is based on the Leuven model and incorporates as many friction characteristics as possible into one model with as few parameters as possible. This GMS model is not only capable of describing the steady state friction behaviour at constant velocity in the sliding regime and the hysteresis behaviour in the pre-sliding regime, but it also takes into account the frictional lag in the sliding regime and the drifting property in the pre-sliding regime. The model is in fact a parallel connection of single state friction models, having all the same input (namely the velocity) and dynamics but with a different set of values for the model parameters. Each single state friction model has a logic state which indicates if the element sticks or slips. The dynamics of each elementary model are determined by the following rules:

- If the elementary model sticks, the state equation is given by:

$$\frac{dF_i}{dt} = k_i v, \quad (2.24)$$

with F_i the hysteresis force, k_i the elementary stiffness of the asperity and ν_i a fraction parameter ($\sum_i \nu_i = 1$).

- If the elementary model slips, the state equation is given by:

$$\frac{dF_i}{dt} = \text{sgn}(v) \nu_i C \left(1 - \frac{F_i}{\nu_i s(v)} \right), \quad (2.25)$$

with C the attraction parameter, which is an indication for the attraction of the friction force to the Stribeck curve $s(v)$.

When a small force is applied to the model all the elements are sticking and the initial stiffness is the sum of all the element stiffnesses $\sum k_i$. An elementary model remains sticking until the force F_i on element i reaches the saturation level ($F_i = \nu_i s(v)$) and element i starts to slip. The elementary model remains slipping until the velocity goes through zero after which it returns to the stick phase. The whole system is in stick when at least one element is still in stick. Conversely, the whole system is in slip when all the elements slip. The total friction force is given as the summation of the outputs of the N elementary state models plus an extra viscous term to account for the viscous friction:

$$F_f(t) = \sum_{i=1}^N F_i(t) + \sigma_2 v(t). \quad (2.26)$$

According to [12], a reasonable value of the number of elementary models (asperities) in order to have a good friction approximation lies between five and twenty.

2.2.3 Friction Model for the Turntable

The stick-slip effect plays a central role in the movement of the turntable. It is therefore very important that a friction model is chosen that can approximate the frictional behaviour accurately. This section has described a literature survey on different friction models with their advantages and disadvantages. Based on this survey two models, static and dynamic, will be chosen. These models are compared and a choice between them will be made.

The most proper static model is the Breedveld model, because from the three mentioned static models it approximates the frictional behaviour most accurately. The GMS model is considered as best dynamic model, because it is an extension of the other mentioned dynamic friction models.

The choice between the Breedveld model and the GMS model is based on the drifting property. In the movement of the turntable, there are a lot of transitions between stick and slip. Due to the large amount of transitions, a lot of (small) oscillations are present during these transitions. It is not desired that a model shows drift due to these oscillations. Figure 2.10 shows a test on the drifting property for the Breedveld model and the GMS model.

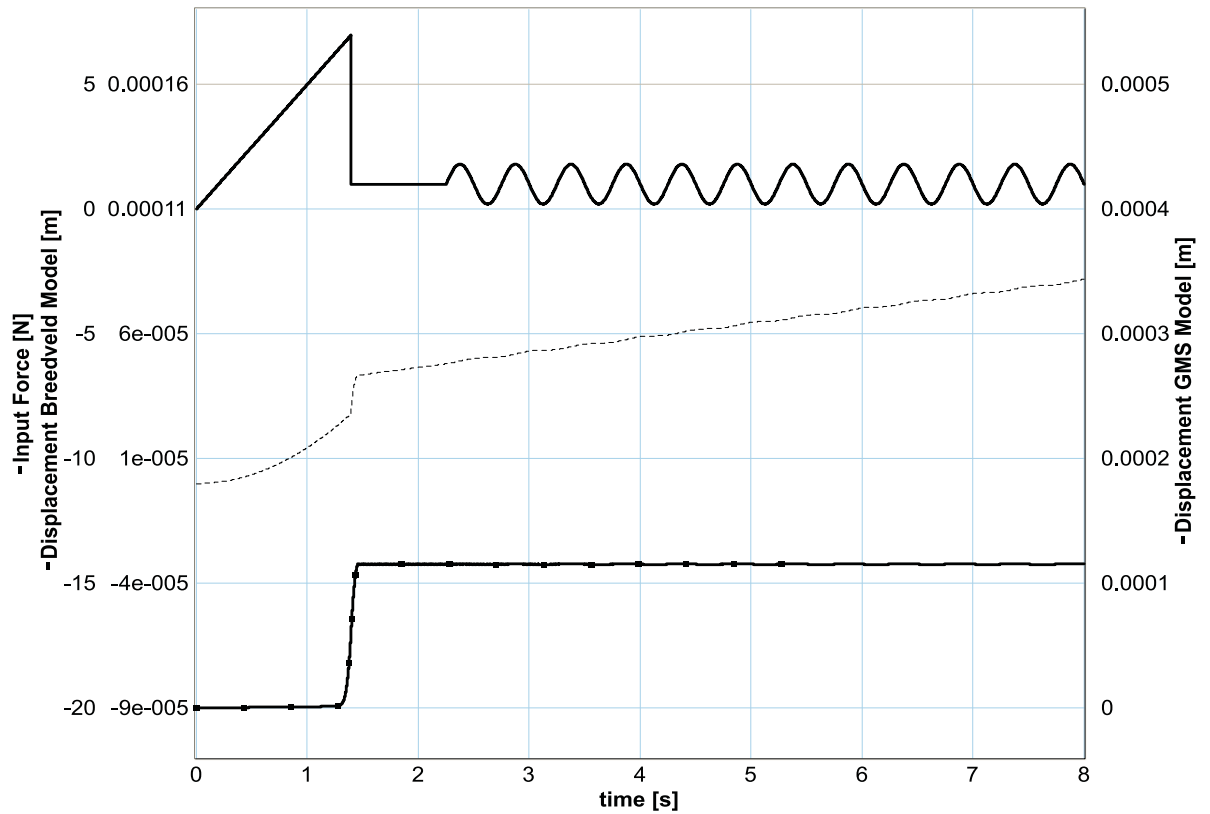


Figure 2.10: Testing the drifting property for two friction models.

A tangential force (upper signal) is applied to an object moving over a flat surface. The objects are first brought into the slip phase and then back into the stick phase with an oscillation on the tangential force. As can be seen in Figure 2.10 the object shows drift in the case of the Breedveld model and no drift the case of the GMS model.

Based on this drifting property, the GMS model will be used in the bond graph model of the turntable.

Chapter 3

20-sim Model

This chapter is about the implementation of the turntable in a model. The model of the turntable has been implemented in 20-sim. The modeling has been done using (screw) bond graphs, which allows the modeling to be done in an energy consistent way. This chapter assumes some basic knowledge about screw bond graphs, a tutorial can be found in [15]. This chapter starts with a description of the geometry of the turntable in Section 3.1. Section 3.2 shows the tube model actuated by piezoelectric elements, followed by a description of the contact model with friction in Section 3.3. The chapter ends with the complete model of the turntable in Section 3.4.

3.1 Geometry

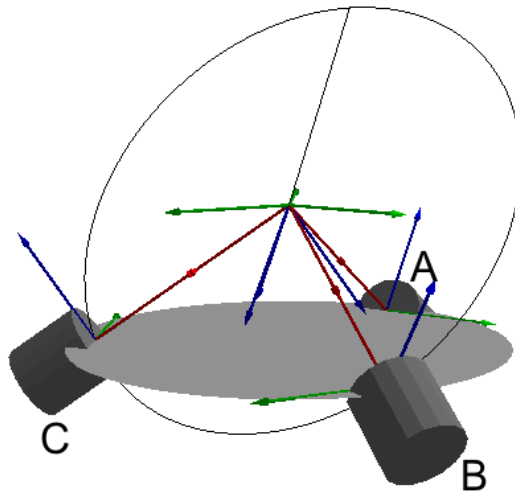


Figure 3.1: Schematic view of the geometry of the turntable.

The geometry of the turntable has already been mentioned in Chapter 2. This section describes the calculation of the different angles, initial transformation matrices and gives a description how to rotate the turntable in a predefined way.

The turntable is supported by three piezoelectric tubes, which are shown as cylinders in Figure 3.1. The central axes from the three tubes join at the top of the figure and are orthogonal. Figure 3.1 furthermore shows a hollow circle and a grey circular surface. The hollow circle is spanned by the contact points of tubes *B* and *C*. Due to the orthogonality,

the normal vector to the surface in the center of the circle corresponds to the central tube axis of tube C . The grey circular surface is spanned by the tops of the tubes and is also shown in Figure 3.2. The angle between the tubes on the circle is 120° and the half angle is defined as β (60°). Furthermore, α is defined as the angle between the central axis of the tubes and the grey circle (Figure 3.2), and $R_{contact}$ is the radius of the grey circle.

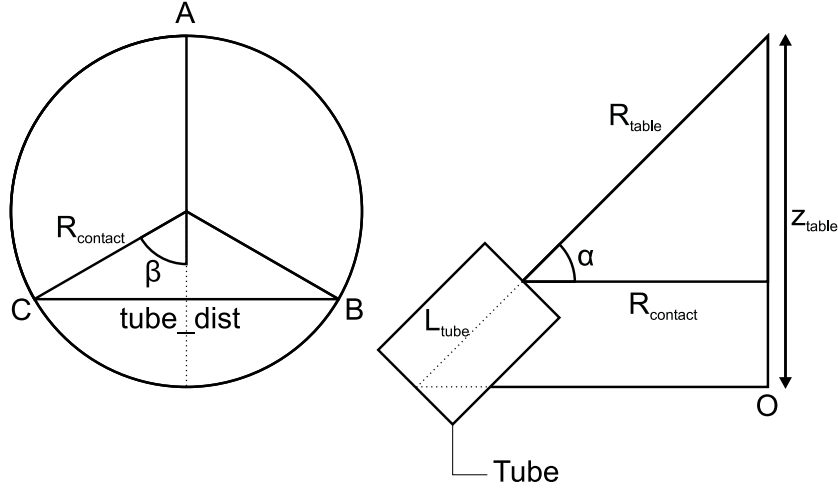


Figure 3.2: Schematic views used for calculations

In order to calculate α , the following relations are defined:

$$\begin{aligned} tube_dist &= \sqrt{2}R_{table} \\ R_{contact} &= \frac{tube_dist}{2 \sin \beta}, \end{aligned} \quad (3.1)$$

where R_{table} and $tube_dist$ are both shown in Figure 3.2. The angle α can now be calculated as:

$$\alpha = \arccos \frac{R_{contact}}{R_{table}}. \quad (3.2)$$

Using α , the distance from the origin O to the top of the table z_{table} can be calculated:

$$z_{table} = R_{contact} \tan \alpha + L_{tube} \sin \alpha. \quad (3.3)$$

The turntable is able to rotate around each of the tube axes (A , B and C in Figure 3.1) as well as around the z -axis. The tubes are positioned such that a rotation around one of the tube axes is achieved by applying a voltage to a quadrant of each of the other two tubes. Figure 3.1 shows a hollow circle perpendicular to axis A and touching the contact points of axis B and C . A rotation around axis A is achieved by actuating a quadrant of B and C in a direction parallel to the perimeter of the circle spanned by the contact points (hollow circle in Figure 3.1). The same holds for a rotation around the other two axes. A rotation around the z -axis is achieved by actuating the two quadrants of each tube, which are not used at the other rotations.

In order to achieve a stable system, the center of mass of the table has to be below the grey circular surface shown in Figure 3.1. Appendix C.3 shows the calculation of the position of the center of mass. The radius of the cross-section of the table at the position of the center of mass is given by $R_{CoM} = \sqrt{\frac{55}{64}}R_{table}$ and can be compared to $R_{contact}$. In the current design of the turntable this radius is given by $R_{contact} = \sqrt{\frac{2}{3}}R_{table}$. This means that the center of mass is above the grey circular surface and is thus not at a stable position.

3.2 Piezoelectric Tube Model

The tubes have been modeled in 20-sim using variable spatial springs actuated by piezoelectric elements. Each tube is sectioned into four quadrants and the quadrants are represented by a spring in combination with a piezoelectric element. The piezoelectric element creates a deflection and changes the length of the spring. By choosing proper stiffnesses and changing the length of the spring along a circular path, the deflection of the piezo causes the tube to bend.

The variable spatial springs are positioned between the fixed world (zero velocity) and a rigid body. A complete description of a variable spatial spring can be found in [16]. The first part of this section is about some basic concepts about the used variable spatial springs. The second part is about the 20-sim model of the tube.

3.2.1 Basic Concepts

This paragraph mentions some basic concepts about the variable spatial springs which will be used to construct the model, and ends with the wrenches generated by the spring. Figure 3.3 shows a spatial spring connecting two bodies B_1 and B_2 , which can be defined in the following way.

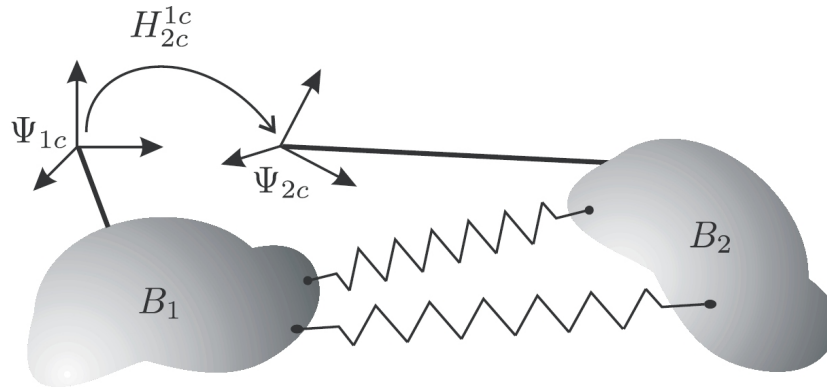


Figure 3.3: Spatial spring and the center of stiffness.

First, two references Ψ_1 and Ψ_2 are defined, rigidly connected to B_1 and B_2 respectively (not shown in the figure). Second, consider the relative position in which the spring has its minimum potential energy. Then, a point in space is chosen, representing the center of stiffness. Two coincident frames Ψ_{1c} and Ψ_{2c} are defined, rigidly connected to Ψ_1 and Ψ_2 respectively. The two frames, Ψ_{1c} and Ψ_{2c} , are coincident only in the center of stiffness.

A bond graph representation of the variable spatial spring is shown in Figure 3.4 and has four power ports:

- $(T_1^{0,0}, W_{1,2}^0), (T_2^{0,0}, W_{2,1}^0)$ corresponding to the hinge points where bodies can be attached to other bodies;
- $(T_l^1, -W_l^1)$ corresponding to the port which can be used to modify the rest configuration of the spring, expressed by H_2^1 in case $H_{2c}^{1c} = I$;
- $(T_c^1, -W_c^1)$ corresponding to the port which can be used to modify the position of the center of stiffness and the principle axis of the spatial stiffness.

Figure 3.5 shows a simple model of a variable spatial spring and will be used to explain the behaviour of the spring. The figure shows four frames which can be moved with respect

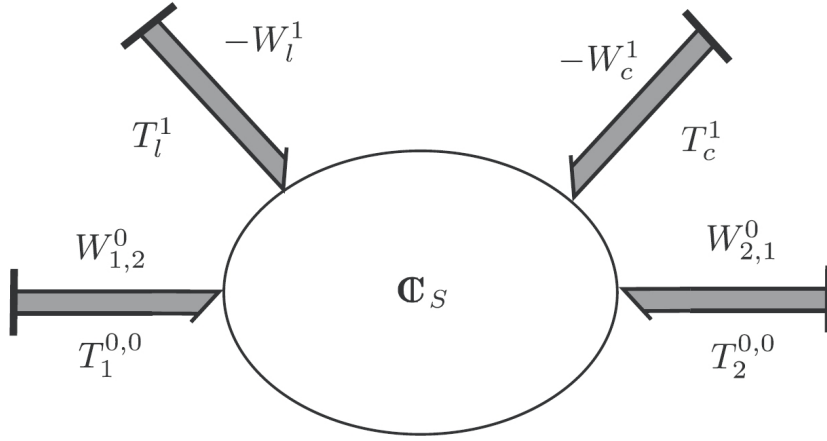


Figure 3.4: Bond graph of variable spring.

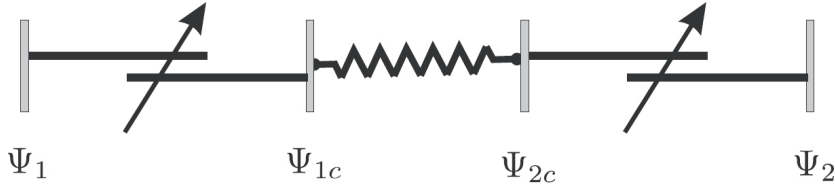


Figure 3.5: Varying spring model.

to each other. Ψ_1 and Ψ_2 are used as hinge points between the outer bodies and the spring. Inside the spring, the length and the center of stiffness can be changed. The change of length is accomplished by changing the relative position between Ψ_1 and Ψ_{1c} and between Ψ_2 and Ψ_{2c} . This change of length will be along a circular path to accomplish the bending the tube. The actual spatial spring is between Ψ_{1c} and Ψ_{2c} .

The twists $T_2^{1,2c}$ and $T_{1c}^{1,1}$ can, according to [16], be calculated from Figure 3.5:

$$\begin{pmatrix} T_{1c}^{1,1} \\ T_2^{1,2c} \end{pmatrix} = \begin{pmatrix} \frac{1}{2}I & I \\ \frac{1}{2}I & -I \end{pmatrix} \begin{pmatrix} T_l^1 \\ T_c^1 \end{pmatrix}. \quad (3.4)$$

The accompanying wrenches can be calculated by transposing the transformations matrix and because $W_{1c,1}^1 = W_{2,2c}^1 = Ad_{H_{1c}^1}^T W_{1c,2c}^{1c}$, the equation for the wrenches becomes:

$$\begin{aligned} W_l^1 &= Ad_{H_{1c}^1}^T W_{1c,2c}^{1c} \\ W_c^1 &= 0. \end{aligned} \quad (3.5)$$

In order to perform the transformation from Ψ_1 to Ψ_{1c} , the transformation matrix H_{1c}^{1c} has to be calculated. This can be done by using Equation 3.4 and the definition of twists:

$$\dot{H}_{1c}^1 = H_{1c}^1 T_{1c}^{1,1} = H_{1c}^1 \left(\frac{1}{2}T_l^1 + T_c^1 \right), \quad (3.6)$$

which can be integrated and inverted to obtain $H_{1c}^{1c}(t)$. The same holds for the transformation matrix H_2^{2c} :

$$\begin{aligned}\dot{H}_2^{2c} &= H_2^{2c} T_2^{2,2c} = H_2^{2c} Ad_{H_1^2} \left(\frac{1}{2} T_l^1 - T_c^1 \right) \\ H_2^{2c} &= \int \dot{H}_2^{2c} dt.\end{aligned}\quad (3.7)$$

To calculate the wrench generated by the spring, the position and orientation of the spring (H_{1c}^{2c}) are used. A full derivation of the relations describing the generated wrench can be found in [14] and the resulting equations are shown below. The wrench has the following form:

$$W_{1c,2c}^{1c}(H_{1c}^{2c}) = \begin{pmatrix} m \\ f \end{pmatrix}, \quad (3.8)$$

where

$$\begin{aligned}\tilde{m} &= 2 as(G_o R_{1c}^{2c}) + as(G_t R_{2c}^{1c} \tilde{p}_{1c}^{2c} R_{1c}^{2c}) + 2 as(G_c \tilde{p}_{1c}^{2c} R_{1c}^{2c}) \\ \tilde{f} &= R_{2c}^{1c} as(G_t \tilde{p}_{1c}^{2c}) R_{1c}^{2c} + as(G_t R_{2c}^{1c} \tilde{p}_{1c}^{2c} R_{1c}^{2c}) + 2 as(G_c R_{1c}^{2c}).\end{aligned}\quad (3.9)$$

$as()$ is an operator which takes the skew-symmetric part of a matrix, R_{1c}^{2c} and p_{1c}^{2c} are the subparts of the matrix

$$H_{1c}^{2c} = \begin{pmatrix} R_{1c}^{2c} & p_{1c}^{2c} m \\ 0 & 1 \end{pmatrix}, \quad (3.10)$$

and G_o, G_t, G_c are called orientational, translational and coupling *co-stiffnesses* of the spring, respectively.

3.2.2 Implementation

This paragraph describes the implementation of the tube model in 20-sim. The tube consists of four quadrants and thus four variable spatial springs. However, in reality the tube is one and the same body. Therefore the four spatial springs on each quadrant are simplified and merged into one spring, which is positioned in the center of the tube. The ports and parameters of this spring are obtained by combining the contributions of each quadrant.

This paragraph first shows a model of the variable spatial spring in 20-sim. After that the model of a tube quadrant is shown, which is based on the variable spatial spring model and is actuated with a piezoelectric element. This paragraph is finalized with the complete model of the tube.

Variable Spatial Spring Model in 20-sim

Figure 3.6 shows the 20-sim model of the variable spatial spring. The spatial spring with input $T_{1c}^{1c,2c}$ associates the wrench that body B_1 applies to the spring ($W_{1c,2c}^{1c}$) to a certain position of the spring H_{2c}^{1c} . In order to calculate the position of the spring, H_{2c}^{1c} , first the accompanying twist ($T_{1c}^{1c,2c}$) has to be calculated, which is the input to the spring.

The twist ($T_{1c}^{1c,2c}$) is the twist of Ψ_{1c} with respect to Ψ_{2c} as a numerical vector expressed in Ψ_{1c} . This twist is calculated by transforming the sum of other twists in the bondgraph model as numerical vectors expressed in Ψ_1 to a twist in Ψ_{1c} . First the twist in Ψ_1 is calculated:

$$T_{1c}^{1,2c} = T_2^{1,2c} + T_0^{1,2} + T_1^{1,0} + T_{1c}^{1,1}, \quad (3.11)$$

which is the same as:

$$T_{1c}^{1,2c} = T_2^{1,2c} - T_2^{1,0} + T_1^{1,0} + T_{1c}^{1,1}. \quad (3.12)$$

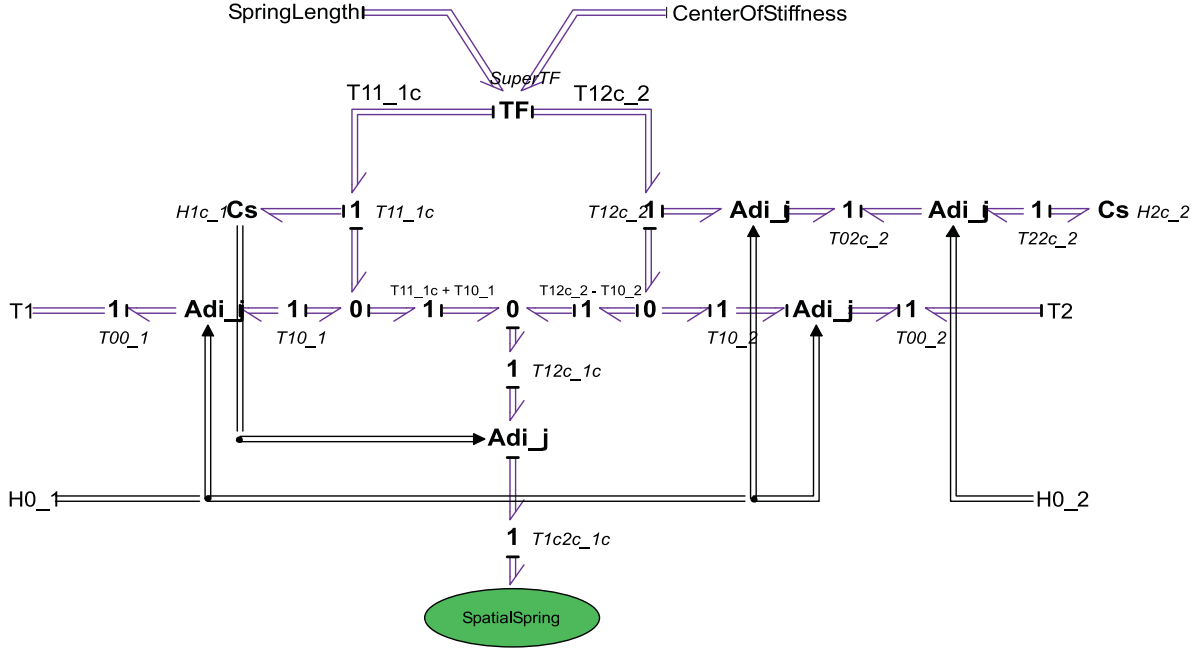


Figure 3.6: Variable spatial spring in 20-sim.

These twists are all available in the variable spring model or can be obtained by transformations. The two incoming twists $T_1^{0,0}$ and $T_2^{0,0}$ can be transformed to $T_1^{1,0}$ and $T_2^{1,0}$ with:

$$T_1^{1,0} = Ad_{H_0^1} T_1^{0,0}, \quad (3.13)$$

and

$$T_2^{1,0} = Ad_{H_0^2} T_2^{0,0}. \quad (3.14)$$

From the expression of the twist $T_{1c}^{1c,2c}$, it is now possible to calculate the state of the spring (H_{1c}^{2c}) by again using the definition of twists:

$$H_{1c}^{2c} = \int \dot{H}_{1c}^{2c} dt = \int H_{1c}^{2c} T_{1c}^{1c,2c} dt. \quad (3.15)$$

This state is used inside the spatial spring element to calculate the generated wrench with Equation 3.8 and 3.9.

Tube Quadrant in 20-sim

The spatial spring in the center of the tube consists of contributions of each quadrant. The model of a tube quadrant is a simplified version of the model of the variable spatial spring described in the previous section. Each quarter calculates the twists T_l^0 and T_c^0 and the transformation matrix H_1^{1c} which are used to calculate the generated wrench in the center of the tube. Figure 3.7 shows the 20-sim model of a quadrant of the tube.

The ‘SuperTF’-element is same as the one used in Figure 3.6 and is described by Equation 3.4 and 3.5. In the model of Figure 3.7 the twist $T_{1c}^{1,1}$ is used for the calculation of the transformation matrix H_1^{1c} by integrating Equation 3.6, which is done inside the ‘Cs’-element. The twists T_l^0 and T_c^0 are obtained by a transformation from the body fixed frame Ψ_1 to the reference frame Ψ_0 with the transformation matrix H_1^0 . The position of the center of stiffness

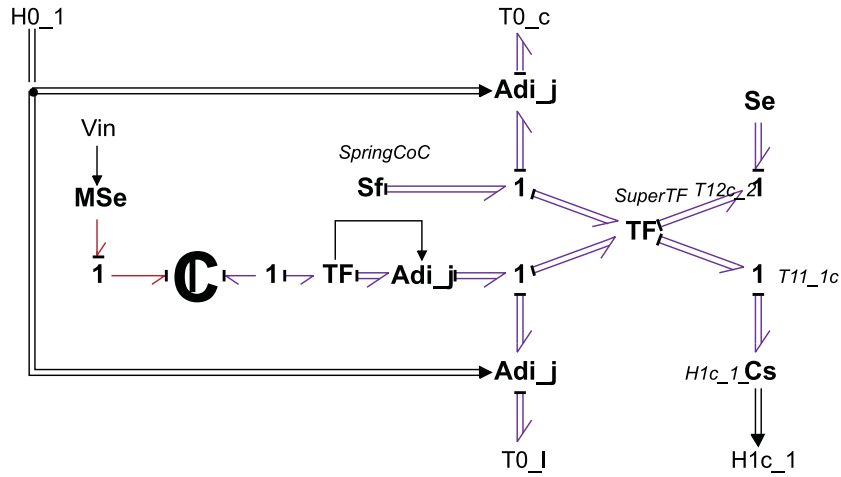
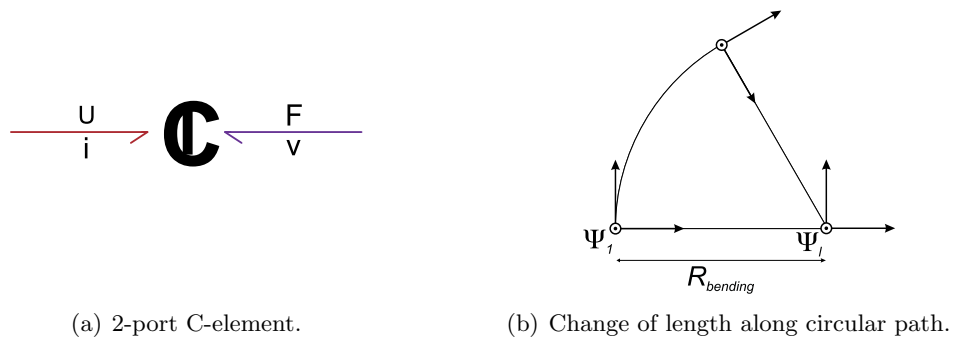


Figure 3.7: 20-sim model of a tube quadrant.

and the principle axis of the spatial stiffness are not changed in this model and the twist T_c^1 is therefore represented by a zero flow source.

By applying a voltage to the piezoelectric element, the length of the element is changed along a circular path. The relations describing the piezoelectric element have already been derived and are shown in Equation 2.2. These relations have been implemented in 20-sim using a 2-port C-element, which is shown in Figure 3.8a.



(a) 2-port C-element.

(b) Change of length along circular path.

Figure 3.8: Elements of tube quarter model.

In order to perform the change of length along a circular path (Figure 3.8b), the model uses a radius of curvature. This radius ($R_{bending}$) has already been calculated and is shown in Equation 2.12. The radius is used to change the ω_x or ω_y component of the twist T_l^1 . Assuming a rotation around the x -axis, the relation is given by:

$$T_l^1 = Ad_{H_l^1} T_l = Ad_{H_l^1} \begin{pmatrix} \frac{1}{R_{bending}} \\ 0 \\ 0 \\ 0 \\ 0 \\ 0 \end{pmatrix} v_{piezo}, \quad (3.16)$$

where v_{piezo} denotes the velocity output of the piezoelectric element.

Complete Tube Model in 20-sim

The complete model of the tube consists of four tube quadrant models and a variable spatial spring element in the center of the tube. Figure 3.9 shows the resulting 20-sim model of the tube, where the left quarter of the tube has been enlarged. The spring element (at the right side of Figure 3.9) contains the model shown in Figure 3.6.

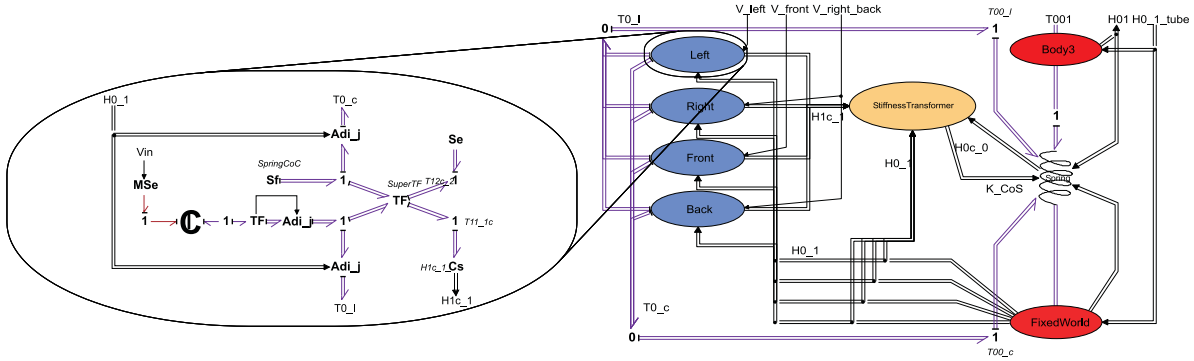


Figure 3.9: Tube model with left quarter enlarged.

The twists T_l^0 and T_c^0 of each quadrant are added and used as input to the spatial spring in the center of the tube. The figure furthermore shows a ‘Stiffness Transformer’ which transforms the stiffness values for each quadrant to a stiffness value for the spatial spring in the center of the tube. This stiffness is calculated once with the initial positions and orientations of the tube quadrants, and the calculation is shown below.

For each variable spatial spring at $t = 0$, the frames Ψ_{1c} and Ψ_{2c} coincide and furthermore (in this model) both represent the position of the center of stiffness. This center of stiffness is (at $t = 0$) represented by Ψ_{0c} . The stiffnesses can be transformed using the transformation matrix from Ψ_{0c} to Ψ_{1c} and is given by:

$$H_{0c}^{1c} = H_1^{1c} H_0^1 H_{0c}^0. \tag{3.17}$$

The stiffness transformation for one of the quadrants is now, according to [14], given by:

$$K_{CoC} = Ad_{H_{0c}^{1c}}^T K Ad_{H_{0c}^{1c}}. \tag{3.18}$$

To get the resulting stiffness in the center of the tube, the sum of the transformed stiffnesses is taken. This stiffness is now used as input to the spatial spring in the center of the tube. This spatial spring (the 20-sim model is shown in Figure 3.6) calculates the generated wrench with Equation 3.8 and 3.9.

3.3 Contact Model with Friction

The contact between the tubes and the turntable is modeled using compliant contacts with friction. A description of a compliant contact model is given in [8]. However, that model does not include friction between the objects in contact. This section first shows basic concepts for the contact model with friction and after that the implementation of the model in 20-sim.

3.3.1 Basic Concepts

The compliant contact model [8] uses a spatial spring to represent the potential energy stored during deformation of the objects and it is assumed that the spring is always present in the case of contact. However, the turntable is driven using the stick-slip effect. This means that once some threshold tangential contact force is reached, the contact is broken (the energy in the spring is lost) and the table starts to slide. First a description of the surface of both objects is needed in order to derive the exact point of contact. Subsequently, the equations for the kinematics are shown followed by a derivation of the position and orientation of the average contact plane. The paragraph ends with some basic concepts on friction.

Both the tube and the turntable are spherical objects (Figure 2.1). The surface of a spherical object can be identified with two parameters, u and v . The parameter v describes a circle in the x - z plane and determines the height on the z -axis of the sphere. Parameter u describes the circle perpendicular to the z -axis with a radius given by $\cos v$. The surface can be identified with a function $f(u, v)$, which assigns a set of coordinates, expressed in a frame rigidly attached to the center of the body, to each point on the surface:

$$f(u, v) = \begin{pmatrix} x(u, v) \\ y(u, v) \\ z(u, v) \\ 1 \end{pmatrix} = \begin{pmatrix} r \cos u \cos v \\ r \sin u \cos v \\ r \sin v \\ 1 \end{pmatrix}. \quad (3.19)$$

The derivative mapping, which gives the tangential vectors to the surface, is given by:

$$f_* = \left(\frac{\partial f}{\partial u} \quad \frac{\partial f}{\partial v} \right). \quad (3.20)$$

In order to get the unit vector normal to the surface, the cross product between the partial derivatives of f is taken:

$$g = \frac{\frac{\partial f}{\partial u} \times \frac{\partial f}{\partial v}}{\left| \frac{\partial f}{\partial u} \times \frac{\partial f}{\partial v} \right|} \quad (3.21)$$

and finally the derivative mapping describing the curvature of the surface:

$$g_* = \left(\frac{\partial g}{\partial u} \quad \frac{\partial g}{\partial v} \right). \quad (3.22)$$

The turntable is preloaded with a spring on top of the table to assure good contact between the tubes and the table. However, the contact model is able to describe the situation in contact as well as the situation with no contact. For the sake of clarity, imagine the table and tube come into contact.

When two objects come into contact, the two surfaces are locally deformed near the contact area. Since both the tube and the table are not infinitely stiff, the contact between these objects is not an ideal point contact, but instead there is an area of contact. However, when the two bodies come into contact, they first touch at a single point. At this moment, a spring is attached with the hinge points at the instantaneous contact points to the bodies B_1 and B_2 (Figure 3.10). Since the hinge points coincide, the spring is initialized with zero energy. When the bodies continue to move with respect to each other, the surfaces of the objects will

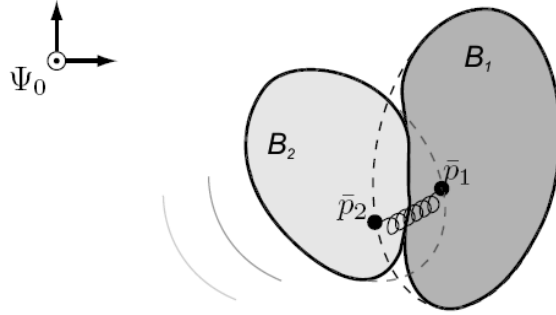


Figure 3.10: Schematic view of two bodies in contact.

deform. This deformation is modeled by moving the hinge points with the objects as if the ideal, rigid shapes were maintained and moving into each other. Since in reality the surfaces of the objects change, this means that the hinge points move away from each other and the spring is loaded. Once the spring force reaches some threshold tangential contact force, the energy in the spring is lost and the table starts to slide.

The kinematics to calculate the velocities of the contact points (hinge points) are described in [8]. The resulting equations are shown below:

$$\begin{aligned} (g_{1*} + H_2^1 g_{2*} H_1^2 (I + \Delta g_{1*})) \dot{p}_1 &= \tilde{T}_2^{1,1} g_1 + H_2^1 g_{2*} (\dot{\Delta} g_2 - \tilde{T}_1^{2,2} p_2) \\ (g_{2*} + H_1^2 g_{1*} H_2^1 (I + \Delta g_{2*})) \dot{p}_2 &= \tilde{T}_1^{2,2} g_2 + H_1^2 g_{1*} (\dot{\Delta} g_1 - \tilde{T}_2^{1,1} p_1), \end{aligned} \quad (3.23)$$

in which $g_* = \hat{g}_* f_*^{-1}$ and $\dot{p} = f_* \dot{u}$. The velocities of the surface parameters (\dot{u}_1 and \dot{u}_2) can now be calculated by multiplying the inverse of the left-side with the right-side. However, the left-side is a four by two matrix and cannot be inverted in the usual sense, but with the Moore-Penrose pseudo inverse [8]: $left^{-1} = (left^T left)^{-1} left^T$.

To calculate the tangential force at the contact surface, first a description of the tangential plane at the contact point has to be defined. The problem is that there are two planes tangent to the surface, one at each hinge point of the spring, which are not aligned in general. To overcome this problem, an average plane somewhere in between these two planes is used. The two planes at the hinge points are defined by the normal vectors to the surfaces (Gauss maps). The exact position of the average tangent plane depends on the relative stiffnesses of the tube and the table and can be computed as described below. The position vector of the average tangent plane is given by:

$$p_c = \frac{k_1 p_1 + k_2 p_2}{k_1 + k_2}, \quad (3.24)$$

where k_1 and k_2 denote the compressibilities of bodies B_1 and B_2 respectively and the normal vector is given by:

$$n_c = \frac{k_1 n_1 - k_2 n_2}{|k_1 n_1 - k_2 n_2|}. \quad (3.25)$$

The transformation matrix H_c^1 can now be computed:

$$H_c^1 = \begin{pmatrix} x_c & y_c & n_c & p_c \\ 0 & 0 & 0 & 1 \end{pmatrix}, \quad (3.26)$$

with x_c being the unit vector pointing in the direction of the first coordinate u of the parametrization and y_c being the unit vector pointing in the direction of the second coordinate v .

The average tangent plane can be used to decompose the twist $T_2^{c,1}$ in components suitable for the friction model. For the stick as well as the slip phase ω_x and ω_y are free. The relative velocity v_z between both bodies perpendicular to the surfaces can be related to the compression force with a 1D spring by $f_z = k_z x_z$. The other degrees of freedom (ω_z , v_x and v_y) are used to calculate the corresponding friction forces with a friction model, implemented at the contact surface. The friction model is the Generalized Maxwell Slip (GMS) model, which has been described in Section 2.2.

3.3.2 Implementation

The contact model has been implemented in 20-sim and is shown in Figure 3.11. This paragraph first explains the submodels used in the model shown in Figure 3.11. After that the implementation of the GMS friction model at the contact surface is shown, followed by a description on how to align the bodies in contact correctly.

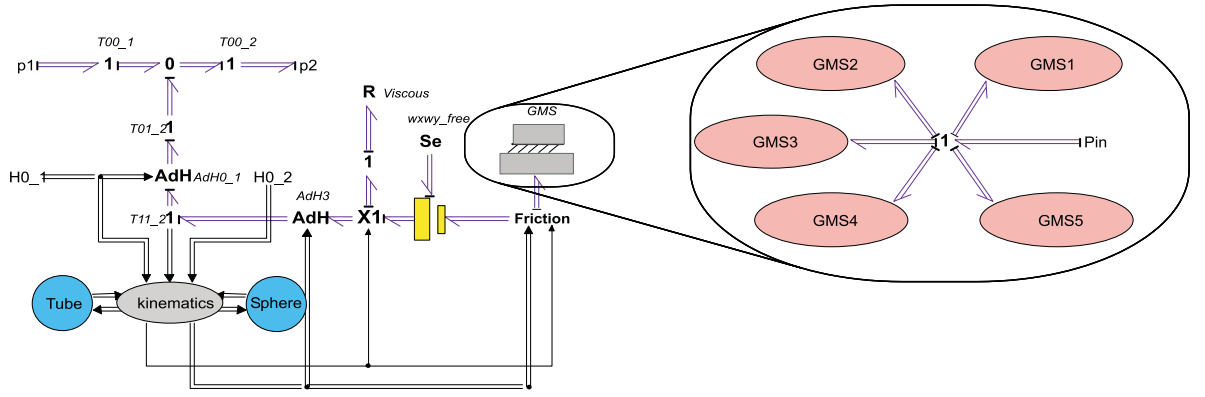


Figure 3.11: Contact model with friction in 20-sim.

Inside ‘kinematics’, the velocities at the contact point (\dot{u} and \dot{v}) and transformation matrix H_c^1 are calculated using Equation 3.23 and 3.26. The transformation matrix H_c^1 , which describes the position and orientation of the average tangent plane, is used to calculate the twist $T_2^{c,1}$ of body 2 with respect to body 1 expressed in the coordinates frame Ψ_c (at the average tangent plane). This twist is decomposed to get the different velocity components at the average tangent plane. The submodel ‘Friction’ decomposes the twist $T_2^{c,1}$ and assigns the correct inputs for the friction model, which will be explained in the next paragraph. Furthermore this submodel calculates the Stribeck curve (Paragraph 2.2.1). The submodel ‘Viscous’ adds a viscous friction force proportional to the velocity.

GMS Friction Model

As mentioned in Paragraph 2.2.3, the GMS model is used to describe frictional behaviour. The velocity inputs to the friction model consist of components of the twist $T_2^{c,1}$. As mentioned at the end of Paragraph 3.3.1, the ω_x and ω_y component are free in the case of stick as well as slip and are therefore not used as input to the friction model. The v_z component is related to the compression force by a 1D spring. The other components are all vectors on the average tangent plane and consist of two translational (v_x and v_y) and a torsional (ω_z) component. The torsional velocity component ω_z is assumed to be zero and not taken as an input to the friction model. The reason for this is that the piezoelectric tubes can not generate torsion at the contact points. This means the velocity input to the friction model consists of a x and

y component (2D), whereas the friction model is a 1D model. Therefore the GMS model is extended to a 2D model which can be used at the contact surface.

The GMS model consists of five submodels, each representing an asperity. The equations for a submodel in case of 1D are shown in Paragraph 2.2.2, Equation 2.24 and 2.25. Each submodel checks if the asperity is sticking or slipping and applies the correct equation, which is integrated to get the friction force. For the 2D case the equations remain the same, except for the force F which becomes $\begin{pmatrix} F_x \\ F_y \end{pmatrix}$, the velocity v which becomes $\begin{pmatrix} v_x \\ v_y \end{pmatrix}$, and the Stribeck curve $s(v)$ which becomes $\begin{pmatrix} s_x(v) \\ s_y(v) \end{pmatrix}$.

Alignment of the Bodies in Contact

In order to let the contact models work properly, it is very important that the initial conditions of both bodies correspond to each other. This means that the initial contact points (u and v) have to correspond to the initial position and orientation of the objects (the H -matrices). This is accomplished by setting $u = v = 0$ and aligning the H -matrices of both bodies. Because $u = v = 0$ means the contact point is at the positive x -axis of the body, the x -axes of both bodies have to be aligned (Figure 3.12). For two tube frames this means a rotation of β around the z -axis and, for all tube frames, a rotation of α around the y -axis. For the table frames, this means the same rotation as the tube frames plus an extra rotation of 180° around the y -axis to align them correctly.

In the section about the geometry of the turntable (Section 3.1), it was mentioned that the direction of actuation of the tubes has to be parallel with the perimeter of the circle in Figure 3.1. To achieve this, the tubes are rotated 45° such that the bending of two tubes causes a rotation around the axis of the third tube (not shown in Figure 3.12).

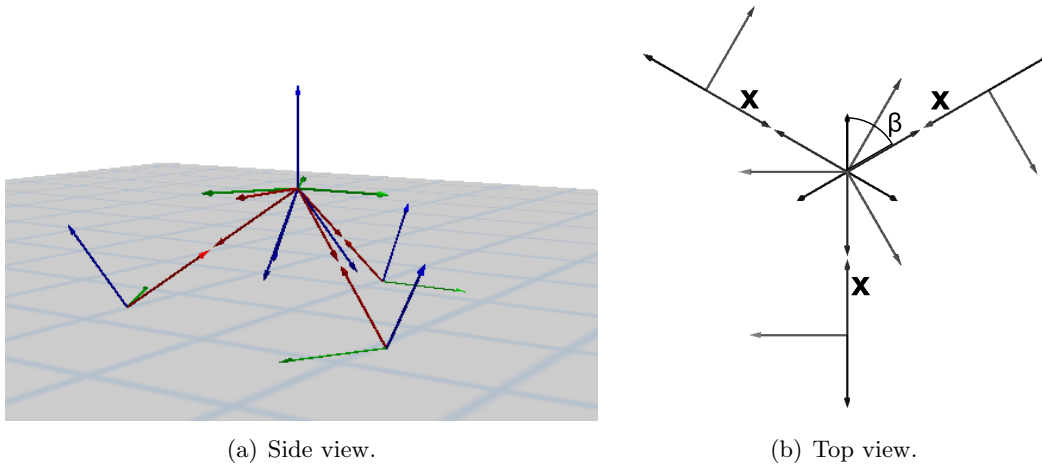


Figure 3.12: Alignment of the tube frames and table frames.

3.4 Complete Model of the Turntable

This section presents the complete model of the turntable, which is shown in Figure 3.13. The figure shows the table (gray circle at the top), three contact models (two circles with a dashed line) and three tubes (springs). The ‘ $x \leftrightarrow z$ ’ submodels between the tubes and the contact models assure the correct alignment of the H matrices. The parameters are declared in the submodel ‘Parameters’ and some calculations are done inside ‘Calculations’.

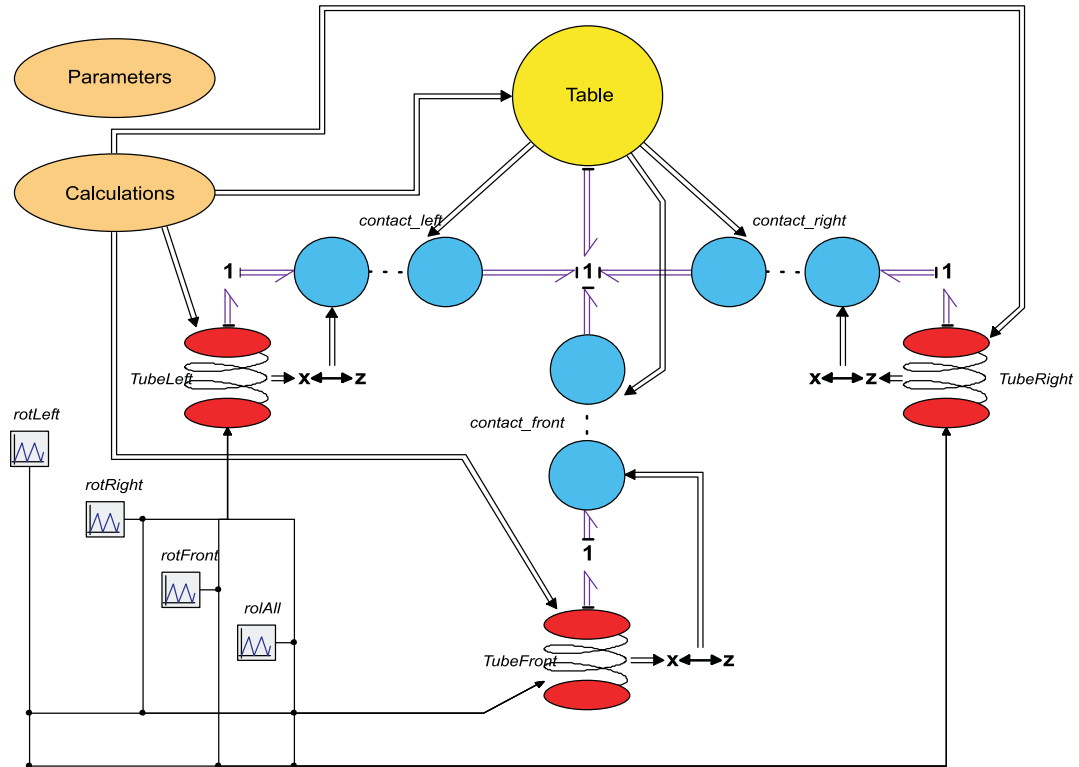


Figure 3.13: Complete model of the turntable in 20-sim.

At the left side of Figure 3.13, four blocks are shown. These blocks generate the actuation signals, which are applied to the tube quadrants. The outputs are sawtooth shaped signals and are characterized by the amplitude, frequency, start time, stop time and relative position of the maximum within the period. As an example, Figure 3.14 shows the output signal at 100 V, 1 Hz, starting at 1 s, stopping at 4 s and the maximum value positioned at $a = 0.95$.

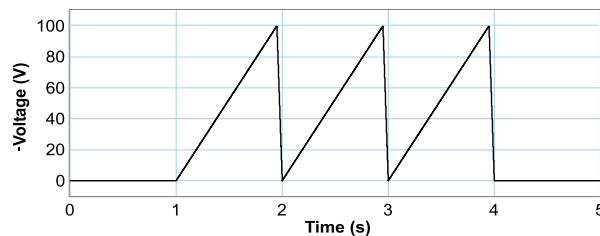


Figure 3.14: Sawtooth shaped actuation signal.

The results of the simulations which have been done with the developed model will be shown in Section 4.2.

Chapter 4

Measurements and Simulations

In order to get some insight in the way the turntable rotates as well as to acquire data for a comparison with the developed model, measurements have been done on the real turntable. In this chapter, measurements as well as some simulations will be described and compared with each other.

4.1 Measurements

As mentioned above, some measurements have been performed on the turntable. A description of the measurement setup is shown in Paragraph 4.1.1. Paragraph 4.1.2 describes a method to adapt the slew-rate of the driving signal. The final section is about the measurements which have been performed on the turntable.

4.1.1 Measurement Setup

The measurements have been done with a laser in combination with a quadrant photodiode. Figure 4.1 shows the setup with the turntable. The laser beam is reflected by a mirror sited on top of the turntable and collected by a quadrant photodiode. During the measurements, the setup is positioned perpendicular to the actuated rotational axis of the turntable. In this case the displacement at the contact surfaces of the tube can be derived from the geometry of the measurement setup shown in Figure 4.1.

The displacement of the laser spot on the photodiodes is calculated with the output voltage V and the sensitivity of the detector S [m/V]: $x_{spot} = V * S$. When the turntable rotates and the angle θ changes by one degree, the spot on the detector changes two degrees due to the reflection at the surface. The angle θ is therefore given by:

$$\theta = \frac{1}{2} \arctan \frac{x_{spot}}{L}, \quad (4.1)$$

where L is the distance between the detector and the reflection point on the table ($L = 0.175$ m) and the displacement of the table becomes:

$$x_{table} = \theta R_{table}. \quad (4.2)$$

In order to perform the measurements, a signal is generated in LabView¹. This signal, which is a voltage between -10 and 10 V, is offered to a high voltage amplifier (HVA 900²). The signal is amplified 45 times at a maximum current of 25 mA. The output of the amplifier is connected to the quadrants of the piezoelectric tubes to be actuated.

¹LabView is a graphical development environment for test, measurement, and control applications developed by National Instruments: <http://www.ni.com/labview/>

²RHK Technology Inc.:<http://www.rhk-tech.com/products/hva900.html>

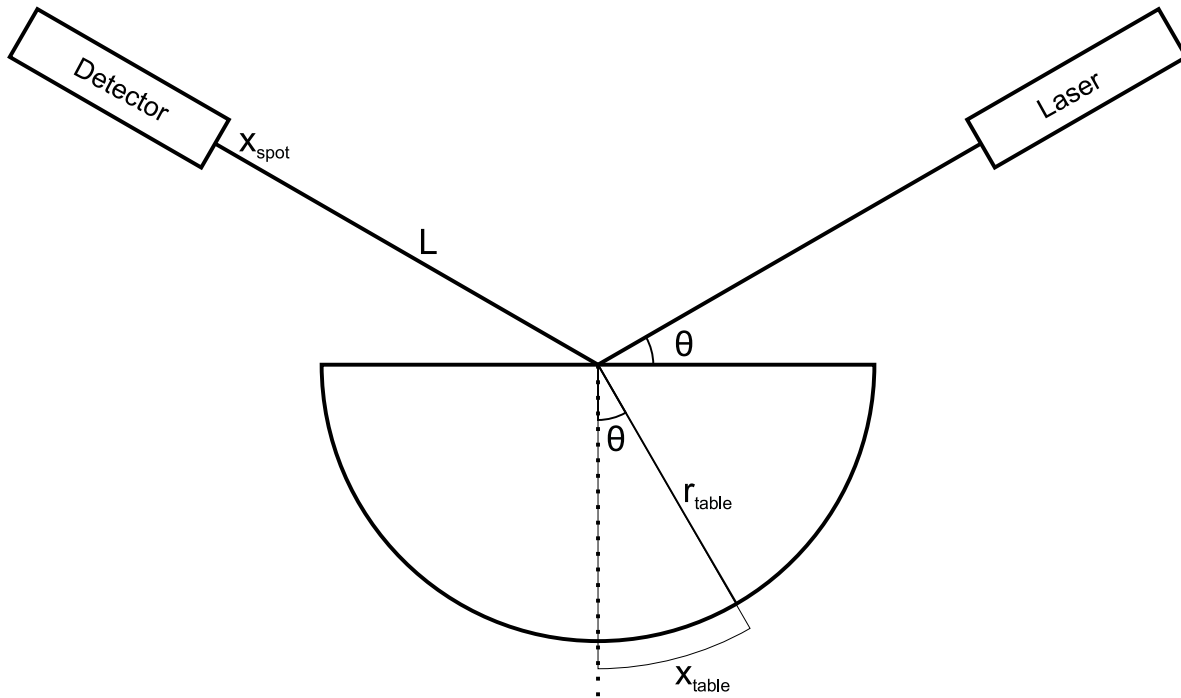


Figure 4.1: Measurement Setup.

4.1.2 Adaptation of the Slew-Rate

The slew-rate SR [V/s] of the driving signal is very important for the ISM mechanism. During the first measurements, the rotation of the turntable at relatively high input voltages was rather poor. The cause of this turned out to be a low slew-rate. Although the slew-rate mentioned in the specifications of the high voltage amplifier (HVA 900) is high enough ($12 V/\mu s$), the measured slew-rate has been found to be only a fraction of this value. The reason for this is that the specified slew-rate only holds at maximum output voltage difference ($900 V$). At smaller voltage differences the time to reach the end-value is the same, and the slew-rate will thus be lower.

The dependence of the slew-rate on the output voltage difference is shown in Figure 4.2. The figure shows the output voltage of the amplifier of three signals where the input jumps due to a step input from $0 V$ to the end value at $t = 20 \mu s$. The upper line shows the output signal at an input which jumps to $3 V$ ($SR = 2.7 V/\mu s$). The other two lines, which are on top of each other, are the amplifier outputs at a jump from 0 to $1 V$ input ($SR = 0.9 V/\mu s$) and an approximation of this signal by dividing the $3 V$ signal by three. Because the approximated signal is (almost) the same as the measured signal, it has been shown that the time to reach the end value is constant and that the slew-rate is proportional to the voltage difference.

The maximum slew rate ($12 V/\mu s$) is reached at the maximum output voltage difference of $900 V$. However, the maximum voltage to drive the piezoelectric tubes is about $200 V$. To obtain a high slew-rate, the input signal to the amplifier is adapted. Figure 4.3 shows an example of the adapted signal.

The applied signal starts at $1 V$. Instead of jumping immediately from 1 to $0 V$, it first jumps to $-1 V$. This means there is a larger difference between the two voltages and therefore the slew-rate will be higher. By jumping to the end value ($0 V$) at the moment the output (almost) reaches the end value, the higher slew-rate ($8.0 V/\mu s$) is achieved. By adapting the voltage differences between the jumps, the slew-rate thus can be varied.

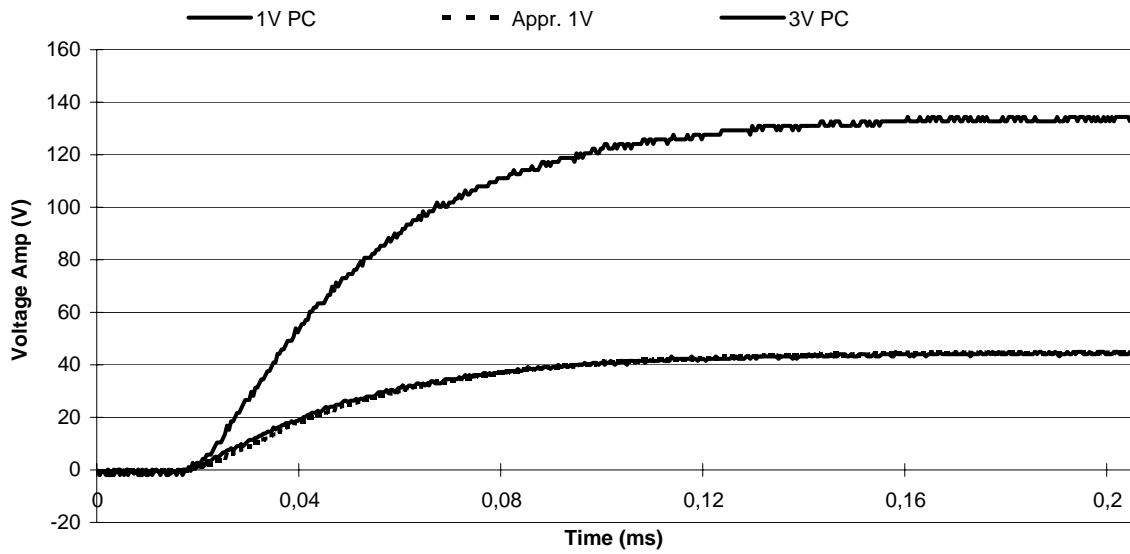


Figure 4.2: Dependence of the slew-rate on the voltage difference.

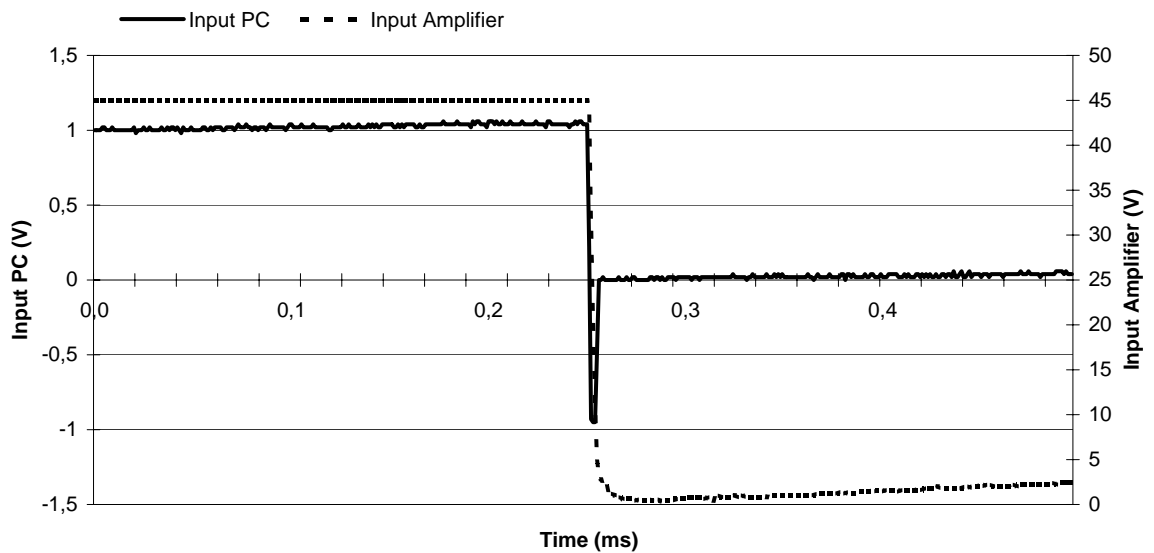


Figure 4.3: Adapted input signal.

4.1.3 Performed Measurements

The measurements performed to acquire data for the validation of the model will be described in this paragraph. The first part of this paragraph is about the determination of the sensitivity of the detector, followed by a description of the results of some measurements that have been performed on the turntable.

Detector Sensitivity

The sensitivity of the detector is determined by moving the detector over a well-known distance and measuring the output voltage. The sensitivity curve of the x -channel is shown in Figure 4.4 and is approximated as $S = 9.9 \cdot 10^{-5} m/V$ in the range between -0.2 and 0.2 mm.

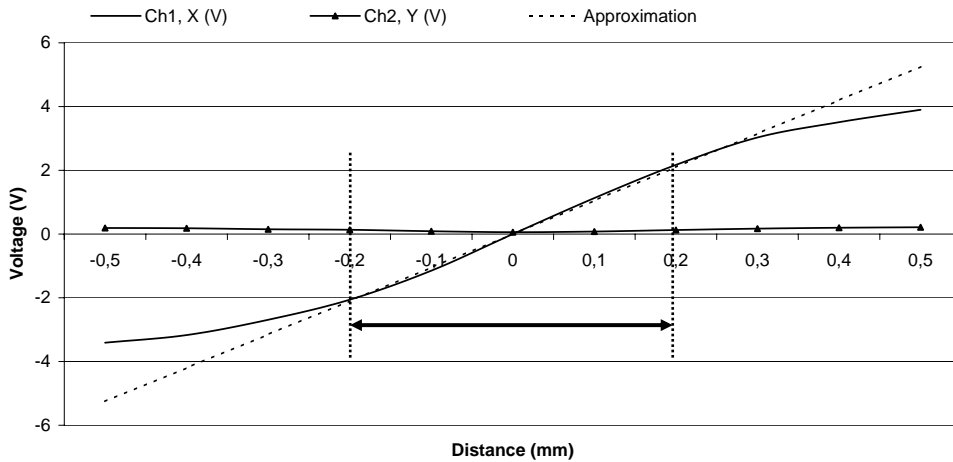


Figure 4.4: Sensitivity of the detector.

Turntable Displacement Measurements

The measurements of the displacement of the turntable have been done at two different input signals, one and two directional. For the sake of clarity, Figure 4.5 shows the idealized input versions in order to get an idea of the types of inputs.

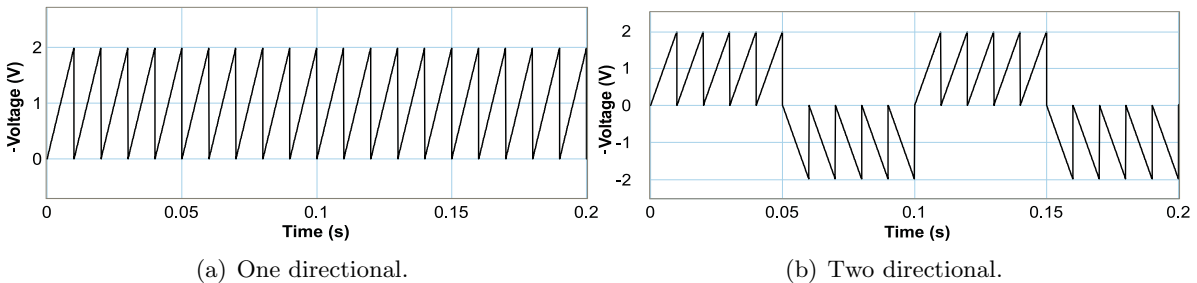


Figure 4.5: Two types of idealized input signals at 2 V and 100 Hz.

As mentioned in Paragraph 4.1.2, during the first measurements the slew-rate of the amplifier was too low to get a reasonable movement of the turntable. In this case, the turntable

‘follows’ the input signal and has no net movement. The measurement results shown in this paragraph have all been achieved with the adapted signal (Figure 4.3) which causes a higher slew-rate of the driving signal.

Figure 4.6 shows the output signal of the detector when the table is rotated around axis B (Figure 3.1) at a two directional amplifier input signal of 2 V and 100 Hz . This signal is amplified 45 times by the high voltage amplifier and offered to the piezoelectric tubes. The net voltage difference between t_1 and t_2 achieved in 5 steps is 0.53 V . Using Equation 4.1 and 4.2, the displacement at the contact surface between tube and table is calculated as $x_{table} = 1.5\text{ }\mu\text{m}$ which means $0.30\text{ }\mu\text{m}$ per step.

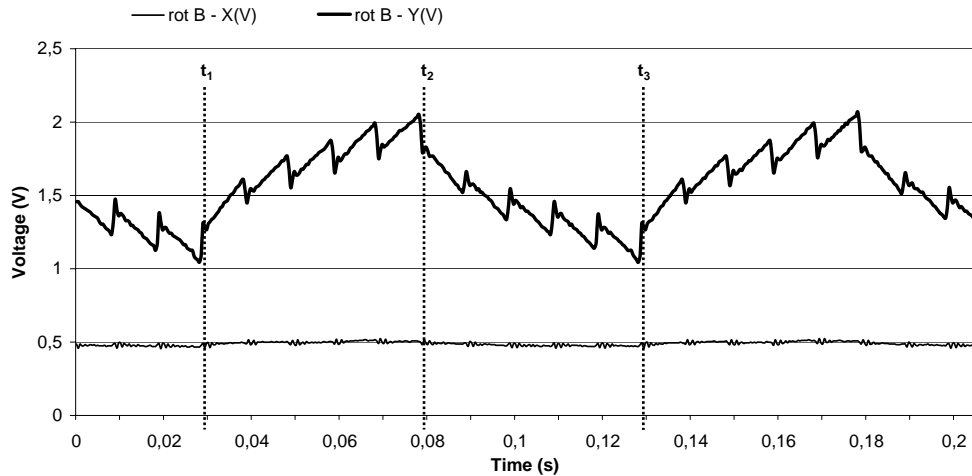


Figure 4.6: Rotation of the turntable around axis B at two directional input.

The output signal at a one directional amplifier input signal of 2 V and 100 Hz is shown in Figure 4.7. The net voltage difference between t_1 and t_2 is 1.19 V achieved in 9 steps. The displacement at the contact surface between tube and table is calculated as $x_{table} = 3.4\text{ }\mu\text{m}$, which means $0.37\text{ }\mu\text{m}$ per step.

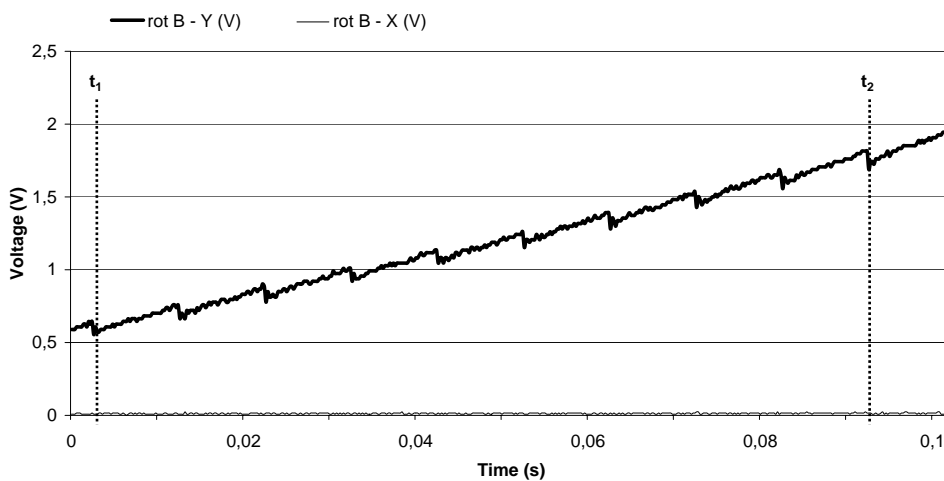


Figure 4.7: Rotation of the turntable around axis B at one directional input.

4.2 Simulations

Some simulations have been done with the developed bond graph model in order to compare the model to the measurements. The different submodels, which have been mentioned in Chapter 3, have all been tested for their functionality. A description of how to determine several parameters of the model is shown in Paragraph 4.2.1. Paragraph 4.2.2 shows the results of some simulations which can be used for comparison with the measurements.

4.2.1 Determination of Model Parameters

The determination of the different parameters of the model developed is shown in this paragraph. The dimensions of the turntable in the simulations do not correspond to the real ones. The cause of this is that when applying the real turntable parameters to the model, the integration method calculates variables as zero due to the numerical accuracy. A solution could be to decrease the stepsize, however the simulation then freezes.

Because of the fact that the new version of the turntable contains shear piezo actuators, the future design of a controller will be based on the turntable with shear piezo actuators. This means the model has to be adapted with the shear piezo actuators instead of the piezoelectric tubes. The parameters of this model have therefore not been tuned to fit the reality optimally, but to approximate the general behaviour of the turntable.

Nevertheless, the determination of the different model parameters remains the same. The parameters for the friction model can be estimated using the following rules. The value of the static friction force between two objects before slipping is given by ($F_{st} = \mu_{st}F_N$). Choose values for the fraction parameter ν_i equally spaced between 0 and 1 such that $\sum_i \nu_i = 1$ with i the number of asperities. The maximum force an asperity can sustain is then given by: $W_i = \nu_i F_{st}$. Then choose the deflections δ_i of each asperity equally spaced between the noise level and the total deflection between the objects just before they start to slip. The stiffness of each asperity can now be calculated with $k_i = \frac{W_i}{\delta_i}$.

The derivation of some other parameters is shown in the appendices. The calculation of the spring constants K_x , K_y , K_z and K_ϕ is shown in Appendix B. The calculations of the masses and mass moments of inertia for the tube and the table are shown in Appendix C.

The values for the parameters used during the simulations can be found in Appendix D.

4.2.2 Performed Simulations

Some simulation results will be shown in this paragraph. As mentioned in the introduction of this section, the different submodels have all been tested for their functionality. However, the results of these simulations will not be shown in this paragraph. This paragraph shows the results of the simulations done with the same input signals as used in the measurements in order to compare the results.

Figure 4.8 shows the simulation result of a rotation around axis B at a one directional input signal (Figure 4.5). Two frames out of the accompanying 3D animation are shown in Figure 4.9.

The simulation result of a rotation around axis B at a two directional input signal is shown in Figure 4.10.

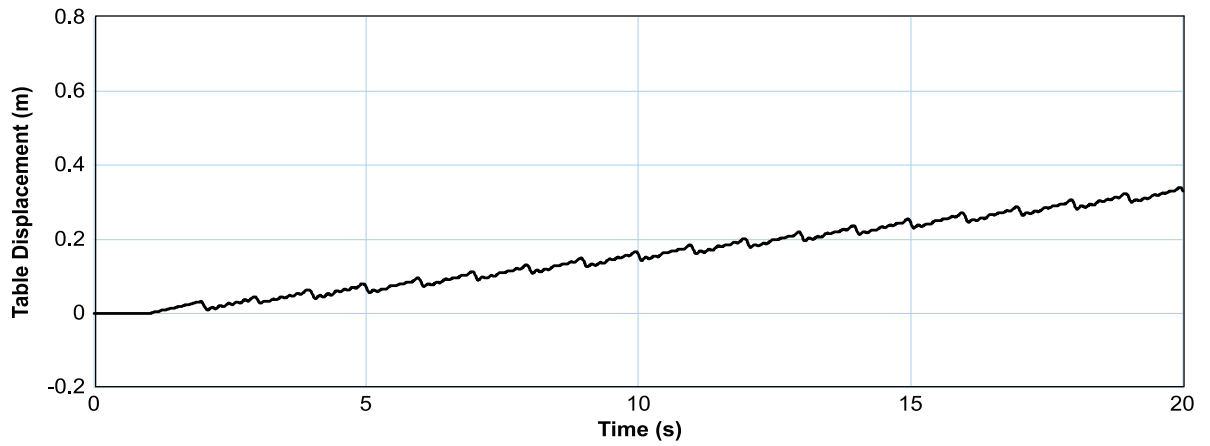


Figure 4.8: Rotation of the turntable around axis B at one directional input.

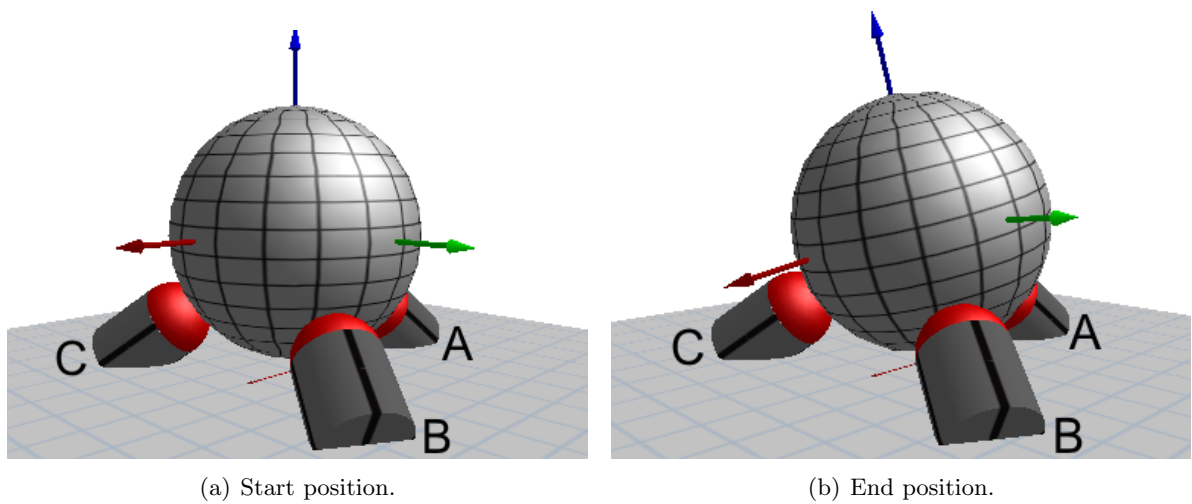


Figure 4.9: Animation showing rotation of the turntable around axis B.

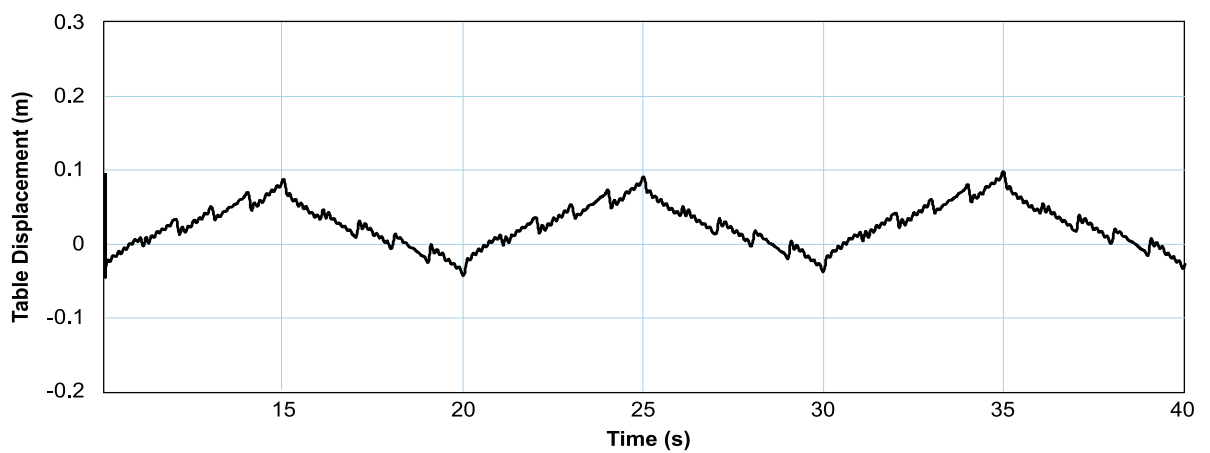


Figure 4.10: Rotation of the turntable around axis B at two directional input.

4.3 Discussion

Although the measurement results can not be compared to the simulation results on a quantitative scale due to the large difference in parameter values, a comparison on a qualitative scale is still possible.

From the measurement result in Figure 4.6, it becomes clear that the turntable returns to its starting position after a two directional input. The voltages at t_1 and t_3 are the same, however there will be a small error influenced by several factors. First of all, the measurement setup has a limited accuracy. The laser beam has to be positioned perpendicular to the rotational axis in order to reduce the crosstalk between the quadrants of the detector. Furthermore the setup is very sensitive to vibrations from the environment. Moreover, the current version of the turntable contains a misalignment in the axes. The axes are not positioned perpendicular with respect to each other, which means the rotations are not exactly around the axis expected. A third possible factor could be that the table and tube surfaces show some form of wear, because the hardness of both materials is limited. This means that after many movements the surface can be flattened out, which influences the stick-slip behaviour.

Although the displacement of the turntable in the simulation result shown in Figure 4.10 is different compared to the results of the measurements, it almost returns to the starting position as well. The differences between the minimum values of cycles is less than 0.5 %. From Figure 4.10 it can be seen that not every step results in the same displacement. This is caused by the number of elementary GMS models which start to slip. At relatively low velocities, more elements are in the stick phase compared to more elements in the slip phase at relatively high velocities.

Although there is a difference between the model parameters and the real parameters, nevertheless it can be concluded that the bond graph model developed is able to approximate the general behaviour of the real turntable.

Chapter 5

Conclusions and Recommendations

5.1 Conclusions

The main goal of this assignment was to develop a simulation model of the piezoelectric turntable used in the $\mu SPAM$ project. The model has been implemented in 20-sim using bond graphs.

The model developed consists of several submodels, which represent the different parts of the turntable. Due to the modular design, the individual submodels can easily be replaced by improved versions. The piezoelectric tubes have been modeled with variable spatial springs. The change of length of these springs is accomplished with piezoelectric elements, which have been modeled as 2-port C-elements. A friction model has been implemented at the contact surfaces between the tubes and the table. The contact surfaces have been modeled as compliant contacts and the GMS model has been chosen as the friction model. The main reason for this model is that it incorporates the drifting property.

Measurements have been done on the turntable for a comparison with simulations. This comparison has been done from a qualitative point of view. Although the dimensions during the simulations do not correspond to the real dimensions, it has been shown that the developed model is able to approximate the general behaviour of the real turntable.

5.2 Recommendations

This report has presented the modeling of a piezoelectric inertial stepping turntable using bond graphs. This section discusses some aspects suitable for further research.

- The current turntable uses piezoelectric tubes for the actuation. The next version of the turntable will use shear piezo actuators, which means the model has to be changed. Due to the modular design of the model, the tube models can be replaced by models of the shear piezo actuators in a straightforward way.
- A future assignment could be the development of a controller for the turntable. This controller will be based on the new design of the turntable, which uses shear piezo actuators. For the design of the controller one could think of using the model knowledge in a fuzzy controller or a feed-forward controller.
- In order to use the current model for the implementation of a controller, a few extra steps have to be taken. Because the states of the model do not correspond to the real states, it is not possible to use them directly in a controller for the turntable. However, by defining a mapping from the real parameters to the model parameters, it is possible

to implement a controller for the model and then use the inverse mapping to control the real turntable.

- The parameters used in the simulations presented do not correspond to the reality. One could search for other ways of implementing the different submodels such that the model can be simulated with parameters that do fit measurements. This way, the simulations can be compared to the measurements on a quantitative instead of a qualitative scale.
- Another point which can be improved is the design of the measurement setup. The current setup uses a laser in combination with a quadrant detector which has to be positioned perpendicular on the rotation axis. An improvement could be a measurement system independent of the rotation axis for more accurate and faster measurements.
- In the current design of the turntable, the center of mass is positioned above the cross-section of the table spanned by the contact points. This means the center of mass is not at a stable position. In order to improve this, the center of mass should be positioned lower. This can be achieved for instance by using two or more materials in the table with the heavier materials at the outer side of the half sphere, or by removing some material from the center of the half sphere. Another way to lower the distance between the center of mass and the plane spanned by the three contact points is by changing the angle between the axes of the tube. A consequence is then, that the axes are not orthogonal and thus the rotation axes do not correspond to the axes of the tube anymore.

Appendix A

Energy Function of the Piezoelectric Element

The total work done on the piezoelectric element consists of an mechanical and an electrical part:

$$dE(z, q) = Fdz + Vdq. \quad (\text{A.1})$$

However, the relations for the piezoelectric element (Equation 2.2) are described in terms of the intensive variables, the efforts F and V . Therefore the co-energy is used:

$$E^*(F, V) = -(E(z, q) - Fz - Vq), \quad (\text{A.2})$$

and for the work done, by substituting Equation A.1:

$$dE^*(F, V) = -(dE(z, q) - Fdz - zdF - Vdq - qdV) = zdF + qdV. \quad (\text{A.3})$$

After substituting Equation 2.2 (where the matrix elements are numbered as a_{ij}), taking the integrals and neglecting the integration constant:

$$\begin{aligned} E^*(F, V) &= \left(\int_{F'=0}^F (a_{11}F' + a_{12}V) dF' \right)_{V=0} + \left(\int_{V'=0}^V (a_{12}F + a_{22}V') dV' \right)_{F=const} \\ &= \frac{1}{2}a_{11}F^2 + \frac{1}{2}a_{22}V^2 + a_{12}FV. \end{aligned} \quad (\text{A.4})$$

The final relation for the co-energy is found by substituting the matrix elements of Equation 2.2:

$$E^*(F, V) = \frac{s_{33}^E L}{2A_m} F^2 + \frac{\epsilon_{11}^T A_e}{2h} V^2 + \frac{d_{31} L}{h} FV. \quad (\text{A.5})$$

Appendix B

Spring Constants of the Tube

The tube has three types of spring constants: bending, elongation and torsional stiffness. To calculate the values for each of them, the area moment of inertia is used. First the polar moment of inertia is defined [18]:

$$I_p = \int_A r^2 dA = \int_A (x^2 + y^2) dA, \quad (\text{B.1})$$

and therefore:

$$I_p = I_x + I_y. \quad (\text{B.2})$$

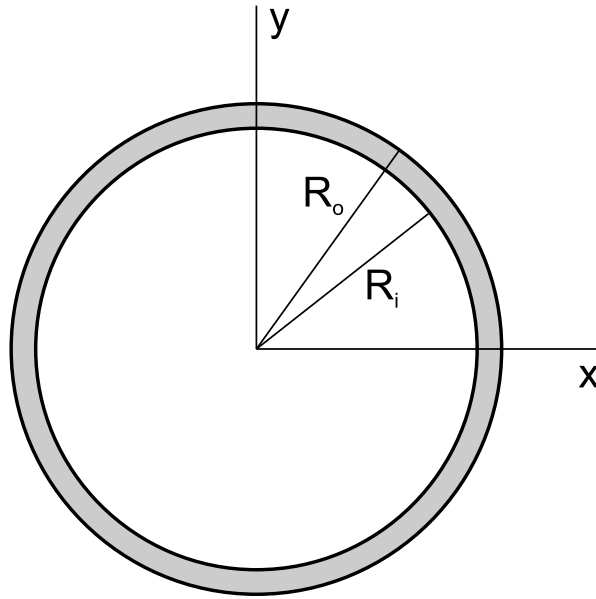


Figure B.1: Top view of the tube.

For the circle in Figure B.1, this means:

$$I_p = \int_A r^2 dA = \int_{R_i}^{R_o} 2\pi r^3 dr = \frac{\pi(R_o^4 - R_i^4)}{2}, \quad (\text{B.3})$$

and for reasons of symmetry:

$$I_x = I_y = \frac{I_p}{2} = \frac{\pi(R_o^4 - R_i^4)}{4}. \quad (\text{B.4})$$

B.1 Bending Stiffness

According to [18], assuming a concentrated load F at $z = L$, the deflection of the tube x at the free-end is given as:

$$x = \frac{FL^3}{3EI_x}, \quad (\text{B.5})$$

and therefore for the bending stiffness of the tube:

$$K_x = K_y = \frac{F}{x} = \frac{3EI_x}{L^3} = \frac{3\pi E(R_o^4 - R_i^4)}{4L^3}. \quad (\text{B.6})$$

B.2 Elongation Stiffness

The elongation of the tube is, according to [18], given by:

$$z = \frac{FL}{EA}, \quad (\text{B.7})$$

and therefore:

$$K_z = \frac{F}{z} = \frac{EA}{L} = \frac{\pi E(R_o^2 - R_i^2)}{L}. \quad (\text{B.8})$$

B.3 Torsional Stiffness

The angle of twist for the tube is given by [18]:

$$\phi = \frac{TL}{GI_p}, \quad (\text{B.9})$$

and therefore for the torsional stiffness:

$$K_\phi = \frac{T}{\phi} = \frac{GI_p}{L} = \frac{\pi G(R_o^4 - R_i^4)}{2L}, \quad (\text{B.10})$$

where E is the Young's modulus, $G = \frac{E}{2(1+\nu)}$ is the shear modulus, $\nu = 0.31$ the Poisson's ratio for the piezoceramic.

Appendix C

Mass Properties

This appendix describes the calculation of the different mass properties of the tube. It starts with the mass of the table and the tubes. After that a derivation of the mass moment of inertia is shown and finally the mass moments of inertia of the table and the tube are given.

C.1 Mass

The mass of a specific body can be calculated by multiplying the density ρ of the material with the volume V . The mass of the table is given by:

$$m_{table} = \rho_{table} V_{table} = \rho_{table} \frac{2}{3} \pi R_{table}^3. \quad (C.1)$$

The tube consists of the piezoelectric cylinder with a sphere of Al_2O_3 on top of it. The radius of the top sphere is the same as the outer radius of the tube R_o . The mass of the tube is therefore given by:

$$\begin{aligned} m_{tube,tot} &= m_{tube} + m_{tubetop} \\ &= \rho_{tube} V_{tube} + \rho_{tubetop} V_{tubetop} \\ &= \rho_{tube} \pi (R_o^2 - R_i^2) L + \rho_{tubetop} \frac{4}{3} \pi R_o^3. \end{aligned} \quad (C.2)$$

C.2 Mass Moment of Inertia

The mass moment of inertia of a specific body is the rotational analog of mass for linear motion and it appears in the relationships for the dynamics of rotational motion. The moment of inertia is defined with respect to a specific rotation axis. The moment of inertia with respect to an axis, is derived from the relation for the angular momentum. The angular momentum of a rigid body is defined as: $L = I\omega$.

The angular momentum of an infinitesimal mass element dm with respect to a chosen origin is given by: $dL \equiv r \times p$, where r is the radius vector to the origin and p is the momentum. With $v \equiv \omega \times r$ this relation can be rewritten to: $dL \equiv r \times (dmv) = dmr \times (\omega \times r)$. The rigid body consists of a continuous distribution of mass and therefore requires an infinite sum of all the point mass moments which make up the whole body. This is accomplished by an integration over all the mass:

$$L = I\omega = \int (r \times (\omega \times r)) dm = \int \tilde{r}(\tilde{\omega}r) dm = \int \tilde{r}(-\tilde{r}\omega) dm = \int \tilde{r}(-\tilde{r})\omega dm, \quad (C.3)$$

and therefore:

$$I = \int \tilde{r}(-\tilde{r}) dm = \int \begin{pmatrix} r_y^2 + r_z^2 & -r_x r_y & -r_x r_z \\ -r_x r_y & r_x^2 + r_z^2 & -r_y r_z \\ -r_x r_z & -r_y r_z & r_x^2 + r_y^2 \end{pmatrix} dm. \quad (C.4)$$

The mass element dm will be expressed in terms of the geometry of the object $dm = \rho dV$, with ρ the density of the material and V the volume of the object. Furthermore there exists a coordinate frame centered in the center of gravity and properly oriented such that the inertia matrix only contains elements on its diagonal. The moments of inertia around the principal axes are therefore given by [21]:

$$\begin{aligned} I_{xx} &= \int_V (r_y^2 + r_z^2) \rho dV \\ I_{yy} &= \int_V (r_x^2 + r_z^2) \rho dV \\ I_{zz} &= \int_V (r_x^2 + r_y^2) \rho dV \end{aligned} \quad (C.5)$$

In general the integration over the volume is performed by integrating along the three perpendicular axes: $dV = dx dy dz$. However, both the tubes and the sphere are spherical elements (Figure 2.1). The integration over the volume is therefore performed using coordinate transformations as will be shown below.

C.2.1 Table Mass Moment of Inertia

In order to calculate the table mass moment of inertia, the integration is performed using spherical coordinates:

$$\begin{aligned} x &= r \sin \phi \cos \theta \\ y &= r \sin \phi \sin \theta \\ z &= r \cos \phi \end{aligned} \quad \Rightarrow \quad dV = \left| \det \frac{\partial(x, y, z)}{\partial(r, \theta, \phi)} \right| dr d\theta d\phi = r^2 \sin \phi \, dr d\theta d\phi. \quad (C.6)$$

The mass moment of inertia for a sphere in its center of mass becomes:

$$I_{xx} = I_{yy} = I_{zz} = \int_0^{2\pi} \int_0^\pi \int_0^{R_{table}} \rho r^4 \sin^3 \phi \, dr d\phi d\theta. \quad (C.7)$$

While Equation C.7 can be used to calculate the mass moment of inertia for a sphere, the same equation can be used to calculate the mass moment of inertia for the table (half sphere). The moment of inertia of the half sphere around the axes passing through the origin of the full sphere becomes:

$$I_{xx} = I_{yy} = I_{zz} = \frac{2}{5} m_{table} R_{table}^2, \quad (C.8)$$

with m_{table} the mass and R_{table} the radius of the table.

C.2.2 Tube Mass Moment of Inertia

The mass moment of inertia for the tubes consists of a contribution of the cylindrical tube and a contribution from the Al_2O_3 ball on top of the tube. The mass moment of inertia for the ball has the same form as Equation C.8. The mass moment of inertia of the tube is calculated with cylindrical coordinates:

$$\begin{aligned} x &= r \cos \theta \\ y &= r \sin \theta \\ z &= z \end{aligned} \quad \Rightarrow \quad dV = \left| \det \frac{\partial(x, y, z)}{\partial(r, \theta, z)} \right| dr d\theta dz = r dr d\theta dz. \quad (C.9)$$

The mass moment of inertia for the tube in the center of mass becomes:

$$\begin{aligned} I_{xx} &= \int_{-L/2}^{L/2} \int_0^{2\pi} \int_{R_i}^{R_o} \rho (r^3 \sin^2 \theta + r z^2) dr d\theta dz \\ I_{yy} &= \int_{-L/2}^{L/2} \int_0^{2\pi} \int_{R_i}^{R_o} \rho (r^3 \cos^2 \theta + r z^2) dr d\theta dz \\ I_{zz} &= \int_{-L/2}^{L/2} \int_0^{2\pi} \int_{R_i}^{R_o} \rho r^3 dr d\theta dz, \end{aligned} \quad (C.10)$$

which can be evaluated as:

$$\begin{aligned} I_{xx} &= \frac{1}{4}m_{tube}(R_o^2 + R_i^2) + \frac{1}{12}m_{tube}L^2 \\ I_{yy} &= \frac{1}{4}m_{tube}(R_o^2 + R_i^2) + \frac{1}{12}m_{tube}L^2 \\ I_{zz} &= \frac{1}{2}m_{tube}(R_o^2 + R_i^2), \end{aligned} \quad (C.11)$$

with the mass of the tube m_{tube} from Equation C.2.

The inertias in Equation C.10 and C.11 are defined in the center of mass. However, in the 20-sim model, all mass is lumped in the top rigid body (the tubetop). In order to calculate the correct mass moment of inertia, the parallel axis theorem [18] is used:

$$I_{par} = I_{com} + m_{tube}R_{par}^2, \quad (C.12)$$

where $R_{par} = \begin{pmatrix} \frac{1}{2}L \\ \frac{1}{2}L \\ 0 \end{pmatrix}$ is the vector to the center of mass for the tube. The correct mass moment of inertia for the piezoelectric tubes of the turntable is therefore:

$$\begin{aligned} I_{xx} &= \frac{1}{4}m_{tube}(R_o^2 + R_i^2) + \frac{7}{12}m_{tube}L^2 \\ I_{yy} &= \frac{1}{4}m_{tube}(R_o^2 + R_i^2) + \frac{7}{12}m_{tube}L^2 \\ I_{zz} &= \frac{1}{2}m_{tube}(R_o^2 + R_i^2). \end{aligned} \quad (C.13)$$

As mentioned at the beginning of this section, the mass moment of inertia of the Al_2O_3 ball on top of the tube has the same form as Equation C.8. The resulting mass moment of inertia for the tube becomes therefore:

$$\begin{aligned} I_{xx} &= \frac{1}{4}m_{tube}(R_o^2 + R_i^2) + \frac{7}{12}m_{tube}L^2 + \frac{2}{5}m_{tubetop}R_o^2 \\ I_{yy} &= \frac{1}{4}m_{tube}(R_o^2 + R_i^2) + \frac{7}{12}m_{tube}L^2 + \frac{2}{5}m_{tubetop}R_o^2 \\ I_{zz} &= \frac{1}{2}m_{tube}(R_o^2 + R_i^2) + \frac{2}{5}m_{tubetop}R_o^2. \end{aligned} \quad (C.14)$$

C.3 Center of Mass of the Table

The rotating table of the turntable consists of a half sphere. In order to calculate the position of the center of mass, Figure C.1 is used.

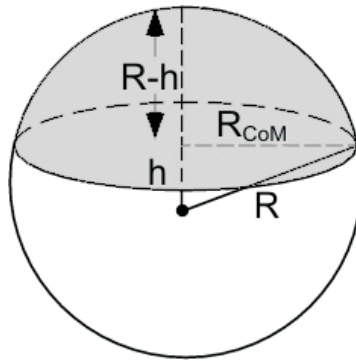


Figure C.1: Sphere used to calculate the moment of inertia.

Figure C.1 shows a sphere with radius R . The distance from the origin of the complete sphere to the geometric centroid h has to be calculated and this can be done by first using Pythagoras:

$$R_{CoM}^2 = R^2 - h^2. \quad (C.15)$$

The distance h can be calculated as [21]:

$$h = \frac{\int_0^R hAdh}{V} = \frac{\int_0^R h\pi R_{CoM}^2 dh}{V} = \frac{\int_0^R h\pi(R^2 - h^2)dh}{V} = \frac{\frac{1}{4}\pi R^4}{\frac{2}{3}\pi R^3} = \frac{3}{8}R. \quad (C.16)$$

Radius R_{CoM} is then given by:

$$R_{CoM} = \sqrt{R^2 - h^2} = \sqrt{\frac{55}{64}}R. \quad (C.17)$$

Appendix D

Parameters

As mentioned in Section 4.2, the parameters used in the simulations do not correspond to the reality. This appendix shows the parameters used for the simulations of the developed model as well as the parameters describing the real turntable. The calculations of values for masses, inertias and spring constants are shown in Appendix B and C.

Table D.1 shows the parameters based on the real dimensions of the turntable.

Table Parameters			Piezoelectric Parameters	
R_{table}	0.01	m	d_{31}	$-210 \cdot 10^{-12} \text{ m/V}$
ρ_{table}	$8.0 \cdot 10^3$	kg/m^3	s_{33}^E	$19.0 \cdot 10^{-12} \text{ m}^2/N$
m_{table}	0.0335	kg	ϵ_{11}^T	$2400 \cdot \epsilon_0 \text{ F/m}$
I_{table}	$1.340 \cdot 10^{-6}$	kgm^2	a	0.95
Tube Parameters				
R_o	$3.175 \cdot 10^{-3}$	m		
R_i	$2.667 \cdot 10^{-3}$	m		
h	$0.508 \cdot 10^{-3}$	m		
L	$6.35 \cdot 10^{-3}$	m		
E	$5.263 \cdot 10^{10}$	N/m^2		
K_x, K_y	$2.471 \cdot 10^7$	N/m		
K_z	$7.728 \cdot 10^7$	N/m		
K_ϕ	253.6	Nm		
$R_{bending}$	$1.570 \cdot 10^4/V$	m		
ρ_{tube}	$7.8 \cdot 10^3$	kg/m^3		
ρ_{ball}	$3.98 \cdot 10^3$	kg/m^3		
m_{tube}	$9.954 \cdot 10^{-4}$	kg		
I_{tube}	$\begin{pmatrix} 1.500 \cdot 10^{-8} \\ 1.500 \cdot 10^{-8} \\ 6.121 \cdot 10^{-9} \end{pmatrix}$	kgm^2		

Table D.1: Parameters describing the real turntable.

Some parameters used in the simulations are the same as the ones used for the measurements. Table D.2 shows the parameters which are different in the simulation or are not shown in Table D.1. The stiffness values shown in Table D.2 have to be put in matrix form in the simulation model. The diagonal terms of the stiffness matrices are given by the table and the off diagonal terms are zero.

Table Parameters		Contact Parameters	
R_{table}	3.15 m	k_1, k_2	1000 N/m
m_{table}	15 kg	$R_{contact}$	2 m
Friction Parameters		Tube Parameters	
k_c	2000 N/m	R_{tube}	1 m
d_c	10 Ns/m	L	2 m
$R_{viscous}$	0 Ns/m	m_{tube}	0.5 kg
F_N	100 N	$K_{o,x}$	100 Nm
μ_{st}	0.3	$K_{o,y}$	100 Nm
μ_c	0.05	$K_{o,z}$	$1 \cdot 10^5$ Nm
C	200 N/s	K_t	$1 \cdot 10^5$ N/m
v_s	0.8 m/s	$R_{bending}$	2 m
δ_{v_s}	2		
k_i	$\begin{pmatrix} 400 \\ 643 \\ 1260 \\ 1350 \\ 1233 \end{pmatrix}$ N/m		
ν_i	$\begin{pmatrix} 0.06 \\ 0.15 \\ 0.21 \\ 0.27 \\ 0.31 \end{pmatrix}$		

Table D.2: Parameters used for the simulations.

Bibliography

- [1] B. Armstrong-Hélouvry, *Control of machines with friction*, Kluwer Academic Publishers, 1991.
- [2] B. Armstrong-Hélouvry, P. Dupont, and C. Canudas de Wit, *A survey of models, analysis tools and compensation methods for the control of machines with friction*, *Automatica* **30** (1994), no. 7, 1083–1138.
- [3] P.A. Bliman, *Mathematical study of the dahl's friction model*, *European Journal of Mechanics A/Solids* **11** (1992), no. 6, 835–848.
- [4] P.C. Breedveld, *An alternative model for static and dynamic friction in dynamic system simulation*, *IFAC-conference on Mechatronic Systems* **2** (2000), 717–722.
- [5] K.J. Astrom C. Canudas de Wit, H. Olsson and P. Lischinsky, *A new model for the control of systems with friction*, *IEEE Transactions on Automatic Control* **40** (1995), no. 3, 419–425.
- [6] PI Ceramic, <http://www.piceramic.com/>.
- [7] C.J. Chen, *Introduction to scanning tunneling microscopy*, Oxford University Press, 1993.
- [8] V. Duindam and S. Stramigioli, *Modeling the kinematics and dynamics of compliant contact*, *International Conference on Robotics and Automation* (2003), 4029–4034.
- [9] P. Dupont, V. Hayward, B. Armstrong, and F. Altpeter, *Single state elasto-plastic friction models*, *IEEE Transactions on Automatic Control* **47** (2002), no. 5, 187–792.
- [10] L. Howald, H. Rudin, and H.J. Guentherodt, *Piezoelectric inertial stepping motor with spherical rotor*, *Rev. Sci. Instruments* **63** (1992), no. 8, 3909–3912.
- [11] D. Karnopp, *Computer simulation of slip-stick friction in mechanical dynamic systems*, *Journal of Dynamic Systems, Measurement and Control* **107** (1985), no. 1, 100–103.
- [12] V. Lampaert, *Modelling and control of dry sliding friction in mechanical systems*, Ph.D. thesis, Katholieke Universiteit Leuven, 2003.
- [13] H. Olsson, K.J. Astrom, C. Canudas de Wit, M. Gaefvert, and P. Lischinsky, *Friction models and friction compensation*, *European Journal on Control* (1997).
- [14] S. Stramigioli, *Modeling and ipc control of interactive mechanical systems: A coordinate-free approach*, Springer, 2001.
- [15] S. Stramigioli and H. Bruyninckx, *Geometry and screw theory for robotics*, 2001.
- [16] S. Stramigioli and V. Duindam, *Variable spatial springs for robot control applications*, *Proceedings of IROS2001* (2001).

BIBLIOGRAPHY

- [17] R. Stribeck, *The key qualities of sliding and roller bearings*, Zeitschrift des Vereines Seutscher Ingenieure **46** (1902), no. 39, 1432–1437.
- [18] S.P. Timoshenko and J.M. Gere, *Mechanics of materials*, 3 ed., PWS-Kent Publishing Company, 1990.
- [19] H. van der Wulp, *Piezo-driven stages for nan positioning with extreme stability*, Ph.D. thesis, Technische Universiteit Delft, 1997.
- [20] J.W. Waanders, *Piezoelectric ceramics - properties and applications*, Philips Components, Eindhoven, The Netherlands, 1991.
- [21] E.W. Weisstein, *Mathworld—a wolfram web resource*, <http://mathworld.wolfram.com/>.